



OPEN

## The improved thermal efficiency of Prandtl–Eyring hybrid nanofluid via classical Keller box technique

Wasim Jamshed<sup>1</sup>, Dumitru Baleanu<sup>2,3,9</sup>, Nor Ain Azeany Moh Nasir<sup>4</sup>, Faisal Shahzad<sup>1</sup>, Kottakaran Soopy Nisar<sup>5</sup>, Muhammad Shoaib<sup>6</sup>, Sohail Ahmad<sup>7</sup> & Khadiga Ahmed Ismail<sup>8</sup>

Prandtl–Eyring hybrid nanofluid (P-EHNF) heat transfer and entropy generation were studied in this article. A slippery heated surface is used to test the flow and thermal transport properties of P-EHNF nanofluid. This investigation will also examine the effects of nano solid tubes morphologies, porosity materials, Cattaneo–Christov heat flow, and radiative flux. Predominant flow equations are written as partial differential equations (PDE). To find the solution, the PDEs were transformed into ordinary differential equations (ODEs), then the Keller box numerical approach was used to solve the ODEs. Single-walled carbon nanotubes (SWCNT) and multi-walled carbon nanotubes (MWCNT) using Engine Oil (EO) as a base fluid are studied in this work. The flow, temperature, drag force, Nusselt amount, and entropy measurement visually show significant findings for various variables. Notably, the comparison of P-EHNF's (MWCNT-SWCNT/EO) heat transfer rate with conventional nanofluid (SWCNT-EO) results in ever more significant upsurges. Spherical-shaped nano solid particles have the highest heat transport, whereas lamina-shaped nano solid particles exhibit the lowest heat transport. The model's entropy increases as the size of the nanoparticles get larger. A similar effect is seen when the radiative flow and the Prandtl–Eyring variable-II are improved.

### List of symbols

$A_1^*$	Prandtl–Eyring parameter-I
$A_2^*$	Prandtl–Eyring parameter-II
$B_\zeta$	Brinkman number
$b$	Initial stretching rate
$C_f$	Drag force
$C_p$	Specific-heat ( $\text{J kg}^{-1} \text{K}^{-1}$ )
$E_\zeta$	Eckert number
EO	Engine Oil
$E_G$	Dimensional entropy ( $\text{J K}^{-1}$ )
$H_\zeta$	Biot number
$h_\zeta$	Heat transfer coefficient
$k$	Porosity of fluid
$\kappa$	Thermal conductivity ( $\text{W m}^{-1} \text{K}^{-1}$ )
$k_\zeta$	Thermal conductivity of the surface
$k^*$	Absorption coefficient
$K_\zeta$	Porous media parameter
$N_\zeta$	Radiation parameter

<sup>1</sup>Department of Mathematics, Capital University of Science and Technology (CUST), Islamabad 44000, Pakistan. <sup>2</sup>Institute of Space Sciences, 077125 Magurele-Bucharest, Romania. <sup>3</sup>Department of Medical Research, China Medical University Hospital, China Medical University, Taichung 40447, Taiwan. <sup>4</sup>Department of Mathematics, Centre for Defence Foundation Studies, Universiti Pertahanan Nasional Malaysia, Kem Sungai Besi, 57000 Kuala Lumpur, Malaysia. <sup>5</sup>Department of Mathematics, College of Arts and Sciences, Prince Sattam Bin Abdulaziz University, Wadi Aldawaser 11991, Saudi Arabia. <sup>6</sup>Department of Mathematics, COMSATS University Islamabad, Attock Campus, Attock, Pakistan. <sup>7</sup>Centre for Advanced Studies in Pure and Applied Mathematics (CASPAM), Bahauddin Zakariya University, Multan 60800, Pakistan. <sup>8</sup>Department of Clinical Laboratory Sciences, College of Applied Medical Sciences, Taif University, P.O. Box 11099, Taif 21944, Saudi Arabia. <sup>9</sup> Department of Mathematics, Cankaya University, Balgat 06530, Turkey. ✉email: wasiktk@hotmail.com; dumitru@cankaya.edu.tr

$N_G$	Dimensionless entropy generation
$Nu_x$	Local Nusselt number
$Pr$	Prandtl number ( $\nu/\alpha$ )
$p$	Column vectors of order $J \times 1$
$q_r$	Radiative heat flux
$q_w$	Wall heat flux
$Re$	Reynolds number
$S$	Suction/injection parameter
$B_1, B_2$	Velocity component in $x, y$ direction ( $m\ s^{-1}$ )
$U_w$	The velocity of the stretching sheet
$V_\zeta$	Vertical velocity
$x, y$	Dimensional space coordinates (m)

### Greek symbols

$\mathcal{T}$	Fluid temperature
$\mathcal{T}_w$	The fluid temperature of the surface
$\mathcal{T}_\infty$	Ambient temperature
$\phi$	The volume fraction of the nanoparticles
$\rho$	Density ( $kg\ m^{-3}$ )
$\sigma^*$	Stefan Boltzmann constant
$\psi$	Stream function
$\Omega$	Independent similarity variable
$\theta$	Dimensionless temperature
$\varepsilon_\zeta$	Relaxation time
$\Lambda_\zeta$	Velocity slip parameter
$\mu$	Dynamic viscosity of the fluid ( $kg\ m^{-1}\ s^{-1}$ )
$\nu$	Kinematic viscosity of the fluid ( $m^2\ s^{-1}$ )
$\alpha$	Thermal diffusivity ( $m^2\ s^{-1}$ )
$\Pi$	Dimensionless temperature gradient

### Subscripts

$f, gf$	Base fluid
$nf$	Nanofluid
$hmf$	Hybrid nanofluid
$p, p_1, p_2$	Nanoparticles
$s$	Particles
SWCNT	Single-walled carbon nanotubes
MWCNT	Multi-walled carbon nanotubes

Liquid mechanics' limits are defined by the thin fluid or liquid layer in contact with the pipe's or an aircraft wing's surface. In the boundary layer, shear forces can damage the liquid. Given that the fluid is in touch with the surface, a range of speeds exists between the maximum and zero boundary layer speeds. Limits on the trailing edge of an aeroplane wing, for example, are smaller and thicker. A thickening of the flow occurs at the front or upstream end of these boundaries. In 1904, Prandtl proposed the concept of boundary layers to describe the flow behaviour of viscous fluid near a solid barrier (see Aziz et al.<sup>1</sup>). Using the Navier–Stokes equations, Prandtl constructed and inferred boundary layer equations for large Reynolds number flows. As a necessary simplification of the original Navier–Stokes equation, the boundary layer theory equations were critical. Studying wall jets, free jets, fluid jets, flow over a stretched platform/surface, and inductive flow from a shrinking plate helps develop the equations for these phenomena. Boundary layer equations are often solved using a variety of boundary conditions that are specific to a given physical model. For a magnetohydrodynamics (MHD) fluid flow with gyrotactic microorganisms, Sankad et al.<sup>2</sup> found that the magnetic and Peclet numbers may be utilised to reduce the thermal boundary layer thickness. After that, Hussain et al.<sup>3</sup> discovered that the thickness of the thermal boundary layer increases as a Casson liquid flows towards the growing porous wedge due to convective heat transfer. The literature has several experiments with various physical parameter impacts on boundary layer flow<sup>4–6</sup> and multiple liquids<sup>7,8</sup>.

A hybrid nanofluid is now attracting the attention of many researchers. Hybrid nanofluids are cutting-edge nanofluids that combine two different types of nanoparticles in a single fluid. The thermal properties of the hybrid nanofluid are better than those of the primary liquid and nanofluids. In machining and manufacturing, hybrid nanofluids are commonly utilised in solar collectors, refrigeration, and coolants. According to Suresh et al.<sup>9</sup>, copper nanoparticles in the alumina matrix mixed at most modest and sufficient levels may preserve the hybrid nanofluid's strength, first introduced in<sup>9</sup>. Despite having a lower thermal conductivity than copper nanoparticles, alumina nanoparticles have excellent chemical inactivity and stability. Yildiz et al.<sup>10</sup> developed an equivalence between theoretical and experimental thermal conductivity models for heat transfer performance in hybrid-nanofluid. In comparison to a mono nanofluid, the hybridisation of nanoparticles improved heat transfer at a lower particle percentage ( $Al_2O_3$ ). Waini et al.<sup>11</sup> investigated a hybrid nanofluid's unsteady flow and heat transfer using a curved surface. As the surface curvature changed, the presence of dual solutions resulted in intensification in the volume percentage of copper nanoparticles. Many years later, Qureshi et al.<sup>12</sup> investigated the hybrid mixed convection nanofluid's characteristics in a straight obstacle channel. They've discovered that

increasing the barrier's radius improves heat transfer by as much as 119%. In addition, the horizontal orientation of the cylinder only supports a heat transfer efficiency of 2.54%. Mabood and Akinshilo<sup>13</sup> investigated the influence of uniform magnetic and radiation on the heat transfer flow of Cu-Al<sub>2</sub>O<sub>3</sub>/H<sub>2</sub>O hybrid nanofluid flowing over the stretched surface. Discoveries such as those made at the science fair show how radiation speeds up heat transport while magnetic forces slow it down. Further hybrid nanofluid studies and experiments have been conducted by these researchers<sup>14–24</sup>.

The Cattaneo–Christov heat flux model describes the heat transfer in viscoelastic flows caused by an exponentially expanding sheet. There may be a relationship between thermal relaxation time and the boundaries of this model. Dogonchi and Ganji<sup>25</sup> researched unstable squeezing MHD nanofluid flow across parallel plates using a Cattaneo–Christov heat flux model some years ago. The thermal relaxation parameter, they found, slowed heat transfer. Additionally, Muhammad et al.<sup>26</sup> discovered that when thermal relaxation increased, the fluid temperature decreased. Other researchers have used the Cattaneo–Christov heat flux model to examine fluid flow and determine the physical features that thermal relaxation affects. Scholars like<sup>27–32</sup> may be found in the literature as examples of this group. Even the temperature of a nanofluid may be reduced by the thermal relaxation parameter, according to Ali et al.<sup>33</sup>. This finding is critical to the contemporary food, medicinal, and aerospace industries. Waqas et al.<sup>34</sup> introduced mathematical modelling using the Cattaneo–Christov model for hybrid nanofluid flow in a rocket engine. The finding exposed that the temperature is reduced when thermal relaxation and melting parameters vary, but the Biot number increases. Other types of hybrids nanofluid characteristics using the Cattaneo–Christov model have been discussed by Haneef et al.<sup>35</sup>. The vital discovery uncovered an escalation causes shrinkage in wall shear stress in momentum relaxation time. Different encounters were found by Reddy et al.<sup>36</sup> in the Cattaneo–Christov model problem for hybrid dusty nanofluid flow. It reveals that dusty hybrid nanofluid has a better heat transfer method than hybrid nanofluid.

Nevertheless, a few years back, a new type of fluid was found called hybrid nanofluid, and many researchers have been eager to search for the characteristics of this type of fluid since then. The research for finding the aspect of non-Newtonian hybrid nanofluid also needed to be done. Latterly, Yan et al.<sup>37</sup> have conducted an investigation towards the rheological behaviour of non-Newtonian hybrid nanofluid for a powered pump. They reported at the highest volume fraction hybrid nanofluid, the viscosity reduced at most 21%. Nabwey and Mahdy<sup>38</sup> are doing an inclusive exploration of micropolar dusty hybrid nanofluid. The finding indicates that the temperature fluctuation in both the micropolar hybrid nanofluid and dust phases is strengthened by increased thermal relaxation. Several investigations have been carried out for the different types of non-Newtonian hybrid nanofluid, such as aluminium alloy nanoparticles by Madhukesh et al.<sup>39</sup>, MWCNT-Al<sub>2</sub>O<sub>3</sub>/5W50 by Esfe et al.<sup>40</sup> and ZnO–Ag/H<sub>2</sub>O by He et al.<sup>41</sup> in the literature. Despite that, only a few research available in the literature investigating the viscoelastic hybrid nanofluid behaviour. Several models can be used to examine the physical properties of the viscoelastic fluid, including the power-law model, the Prandtl fluid model, and the Prandtl–Eyring model. The power-law model predicts the non-linear relationship between deformation rate and shear stress. It has been hypothesised that shear stress is connected to the sine inverse function of deformation rate by the Prandtl model and that it is related to the hyperbolic sine function of deformation rate by the Prandtl–Eyring model. Hussain et al.<sup>42</sup> have investigated the physical aspect of MHD Prandtl–Eyring fluid flow and reported that at all positions in the flow domain, a substantial rise in momentum transportation had been seen against an increase in the fluid parameter. Rehman et al.<sup>43</sup> added in the findings that Prandtl–Eyring liquid particles are subjected to drag forces in a flow when their skin friction coefficients are high (or low). A similar discovery has been conveyed by Khan et al.<sup>44</sup> which the skin friction improves for the Prandtl–Eyring nanofluid. Later, Akram et al.<sup>45</sup> model a MHD Prandtl–Eyring nanofluid peristaltic pumping in an inclined channel. This study demonstrates that the wall tension and mass parameters have a rising influence on axial velocity, whereas the wall damping parameter has a decreasing impact. Li et al.<sup>46</sup> have explored the entropy of the Prandtl–Eyring fluid flow model over a rotating cone. The result demonstration the velocity and temperature have been shown to behave differently when the viscosity parameter increases in magnitude. Latest study for the Prandtl–Eyring hybrid nanofluid model being carried out by Jamshed et al.<sup>47</sup>. The outcome was mentioning the entropy upsurged with radiative flux and Prandtl–Eyring parameter.

The famous numerical technique for solving non-linear boundary layer equations in fluid mechanics is derived by Keller and Cebeci<sup>48</sup> called Keller Box Method (KBM). It is being popularised by Cebeci and Bradshaw<sup>49</sup>. The technique is known for highly accurate and time computation in solving non-linear problems. A lot of investigations of fluid dynamics have been solved using KBM in the literature. Bilal et al.<sup>50</sup> implemented the KBM for solving Williamson fluid flow towards a cylindrical surface and found the results are comparable with other published results. Similar numerical computation was reported by Swalmeh et al.<sup>51</sup> in solving the micropolar nanofluid over a solid sphere using KBM. The computed solution being reported as having a good agreement with the solution computed by `bvp4c` (MATLAB). The KBM is a universal solver since it is proven can solve another type of mathematical modelling, for instance, Carreau fluid model (Salahuddin<sup>52</sup>), micropolar fluid (Singh et al.<sup>53</sup>), viscous fluid model (Bhat and Katagi<sup>54</sup>), Prandtl nanofluid (Habib et al.<sup>55</sup>), MHD nanofluid (Zeeshan et al.<sup>56</sup>) and third-grade nanofluid (Abbasi et al.<sup>57</sup>).

Size and distribution descriptors should be chosen to offer the most significant discrimination for particulate quality concerning specific attributes or characterisation of a manufacturing process, depending on their use. If particle form affects these attributes, the shape and distribution of the particles should be studied in addition to their size. Qualitative terminology like fibres or flakes can be used, or quantitative terms like elongation, roundness, and angularity can also be used. Other quantitative terms include percentages of certain model forms and fractal dimensions. Despite the importance of the particle shape, only a few research can be found in the literature, such as<sup>58–60</sup>. The latest research has been done by Sahoo<sup>61</sup>, which claimed that the particle shapes heavily influence the thermo-hydraulic performance of a ternary hybrid nanofluid. Similar findings have been illustrated by Elnaqeeb et al.<sup>62</sup> in hybrid nanofluid flow with the impact of suction and stretching surface.

Meanwhile, Rashid et al.<sup>63</sup> suggested that the temperature and Nusselt number profiles demonstrate the sphere shape nanoparticles have superior temperature disturbance and heat transmission on hybrid nanofluid flow with the influence of relevant factors.

A few publications have examined the impact of the porosity material, viscid dissipative flow, Cattaneo–Christov heat flow and thermal radiative flow shape-factor along the elongated surface using nanofluid Tiwari–Das type on P-EHNF entropy generation. However, none of these papers has addressed these issues. In the Tiwari–Das (monotonic model), the fluid, speed, and temperature are all the same. As a result, the model is simpler and easier to solve when using the single-phase technique numerically. However, this technique has the drawback of resulting in numerical effects that differ from experimental results in some cases. Nanoparticle concentrations in this model volume range from 3 to 20%. Numerical results could only mimic the effects of SWCNT–EO, MWCNT–EO hybrids, and conventional nanofluids in this study. Thus, in order to bridge the gap, the current research focuses on the solid–fluid characteristics impacts and the level of chaos in the boundary layer using the Keller-box technique of P-EHNF.

## Flow model formulations

The mathematical flow equations shows the moved horizontal plate with the irregular expanding velocity<sup>64</sup>:

$$U_w(x, t) = bx, \quad (1)$$

where  $b$  is an original expanding ratio. Sequestered surface heat is  $\Upsilon_w(x, t) = \Upsilon_\infty + b^*x$  and for the suitability, it is presumed to stand at  $x = 0$ , where  $b^*$ ,  $\Upsilon_w$ , where  $\Upsilon_\infty$  signify the temperature variation amount, heat of surface, and surrounds correspondingly. The plate is supposed to be slippery, and the surface is subjected to a temperature variation.

Primary addition SWCNT nano solid-particles synthesise the hybrid nanofluid in the EO-based liquid at an interaction volume fraction ( $\phi_{ST}$ ) and it is fixed at 0.09 during the examination. MWCNT nano molecules have been extended in combination to obtain a hybrid nanofluid at the concentrated size ( $\phi_{MT}$ ).

**Prandtl–Eyring fluid stress tensor.** Prandtl–Eyring fluid stress tensor is given in the following mathematical form (for example, Mekheimer and Ramadan<sup>65</sup>).

$$\tau = \frac{A_d \text{Sin}^{-1} \left[ \frac{1}{C} \left( \frac{\partial B_1}{\partial y} \right)^2 + \left( \frac{\partial B_1}{\partial y} \right)^{2\frac{1}{2}} \right]}{\left[ \left( \frac{\partial B_1}{\partial y} \right)^2 + \left( \frac{\partial B_1}{\partial y} \right)^{2\frac{1}{2}} \right]} \left( \frac{\partial B_1}{\partial y} \right).$$

Here the curving velocity indicates the mechanisms  $\overleftarrow{B} = [B_1(x, y, 0), B_2(x, y, 0), 0]$ .  $A_d$  and  $C$  is fluid parameters.

**Suppositions and terms of system.** The following principles, as well as the constraints, apply to the flow system:

2-D laminar time-dependent curving	Domenating-layer approximations
Single phase (Tiwari–Das) scheme	Non-Newtonian P-EHNF
Porous medium	Cattaneo–Christov heat flux
Thermal radiative flow	Viscid dissipative flowing
Nano solid-particles shape-factor	Porousness elongated surface
Slippery boundary constraints	Thermal jump boundary constraints

**Formal model.** The formal (geometric) flowing model is displayed as (Fig. 1):

**Model equations.** The constitutive flow formulas<sup>66</sup> of the viscous Prandtl–Eyring hybrid nanofluid, in combination with a porous material, Cattaneo–Christov heat flux and thermal radiative flow utilising the approximate boundary-layer are

$$\frac{\partial B_1}{\partial x} + \frac{\partial B_2}{\partial y} = 0, \quad (2)$$

$$B_1 \frac{\partial B_1}{\partial x} + B_2 \frac{\partial B_1}{\partial y} = \frac{A_d}{C \rho_{hnf}} \left( \frac{\partial^2 B_1}{\partial y^2} \right) - \frac{A_d}{2C^3 \rho_{hnf}} \frac{\partial^2 B_1}{\partial y^2} \left[ \left( \frac{\partial B_1}{\partial y} \right)^2 \right] - \frac{\mu_{hnf}}{\rho_{hnf} k} B_1, \quad (3)$$

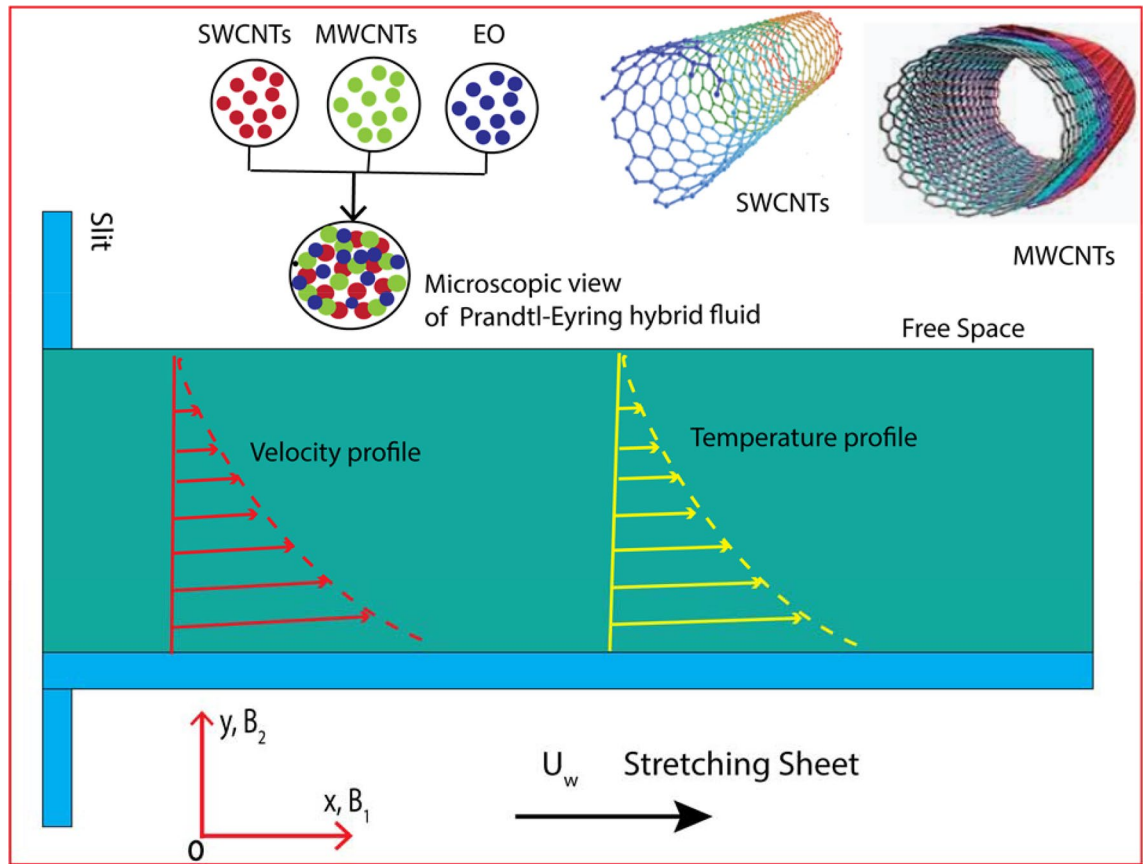


**Figure 1.** Diagram of the flow model.

$$\begin{aligned}
 B_1 \frac{\partial \Psi}{\partial x} + B_2 \frac{\partial \Psi}{\partial y} &= \frac{1}{(\rho C_p) \kappa_{hmf}} \left[ k_{hmf} \left( \frac{\partial^2 \Psi}{\partial y^2} \right) + \mu_{hmf} \left( \frac{\partial B_1}{\partial y} \right)^2 - \frac{\partial q_r}{\partial y} \right], \\
 -\delta^* \left[ B_1 \frac{\partial B_1}{\partial x} \frac{\partial \Psi}{\partial x} + B_2 \frac{\partial B_2}{\partial y} \frac{\partial \Psi}{\partial y} + B_1 \frac{\partial B_2}{\partial x} \frac{\partial \Psi}{\partial y} + B_2 \frac{\partial B_1}{\partial y} \frac{\partial \Psi}{\partial x} + B_1^2 \frac{\partial^2 \Psi}{\partial x^2} + B_2^2 \frac{\partial^2 \Psi}{\partial y^2} + 2B_1 B_2 \frac{\partial^2 \Psi}{\partial x \partial y} \right].
 \end{aligned} \tag{4}$$

the appropriate connection conditions are as follows, which can be located in Aziz et al.<sup>67</sup>:

$$B_1(x, 0) = U_w + N_s \left( \frac{\partial B_1}{\partial y} \right), \quad B_2(x, 0) = V_s, \quad -k_s \left( \frac{\partial \Psi}{\partial y} \right) = h_s (\Psi_w - \Psi), \tag{5}$$

$$B_1 \rightarrow 0, \quad \Psi \rightarrow \Psi_\infty \quad \text{as } y \rightarrow \infty. \tag{6}$$

We formulate the  $\Psi$  as a fluid heat. Other vital parameters are surface permeability  $V_s$ , heat transfer coefficient  $h_s$ , porosity ( $k$ ) and heat conductivity of firm  $k_s$ . Physical features identical, Convective animated surface experienced its heat loss through conductive (Newtonian thermal) and flowing swiftness close to the sheet is comparative to the cut stress exerts in it (slippy form) are deliberate.

**Heat-physical possessions of P-ENF.** Nano solid particles dispersed in EO induce improved thermo-physical characteristics. The next Table 1 equations summarize P-ENF substance variables<sup>68,69</sup>.

$\phi$  is the nano solid-particle size coefficient.  $\mu_f, \rho_f, (C_p)_f$  and  $\kappa_f$  are dynamical viscidness, intensity, functioning thermal capacity, and thermal conductivity of the standard fluid, respectively. The additional characteristics  $\rho_s, (C_p)_s$  and  $\kappa_s$  are the concentration, effective heat capacitance, and heat conductance of the nano molecules, correspondingly.

**Thermo-physical properties of P-EHNF.** The primary assumption of hybrid nanofluids is the suspension of two distinct forms of nano solid particles inside the basis fluid<sup>70</sup>. This assumption improves the capacity for heat transmission of common liquids and is a higher heat interpreter than nanofluids. P-EHNF variables content is summarised in Table 2<sup>71,72</sup>.

In Table 2,  $\mu_{hmf}, \rho_{hmf}, \rho(C_p)_{hmf}$  and  $\kappa_{hmf}$  are mixture nanofluid functional viscidness, concentration, exact thermal capacitance, and thermal conductance.  $\phi$  is the volume of solid nano molecules coefficient for mono

Features	Nano liquid
Dynamical viscidness ( $\mu$ )	$\mu_{nf} = \mu_f (1 - \phi)^{-2.5}$
Density ( $\rho$ )	$\rho_{nf} = (1 - \phi)\rho_f - \phi\rho_s$
Heat capacity ( $\rho C_p$ )	$(\rho C_p)_{nf} = (1 - \phi)(\rho C_p)_f - \phi(\rho C_p)_s$
Thermal conductivity ( $\kappa$ )	$\frac{\kappa_{nf}}{\kappa_f} = \left[ \frac{(\kappa_s + (m-1)\kappa_f) - (m-1)\phi(\kappa_f - \kappa_s)}{(\kappa_s + (m-1)\kappa_f) + \phi(\kappa_f - \kappa_s)} \right]$

**Table 1.** Thermo-physical features for nano liquids.

Features	Hybrid nanofluid
Viscidness ( $\mu$ )	$\mu_{hnf} = \mu_f (1 - \phi_{ST})^{-2.5} (1 - \phi_{MT})^{-2.5}$
Density ( $\rho$ )	$\rho_{hnf} = [(1 - \phi_{MT})\{(1 - \phi_{ST})\rho_f + \phi_{ST}\rho_{p1}\}] + \phi_{Go}\rho_{p2}$
Heat capacity ( $\rho C_p$ )	$(\rho C_p)_{hnf} = [(1 - \phi_{MT})\{(1 - \phi_{ST})(\rho C_p)_f + \phi_{ST}(\rho C_p)_{p1}\}] + \phi_{MT}(\rho C_p)_{p2}$
Thermal conductivity ( $\kappa$ )	$\frac{\kappa_{hnf}}{\kappa_{gf}} = \left[ \frac{(\kappa_{p2} + (m-1)\kappa_{gf}) - (m-1)\phi_{ST}(\kappa_{gf} - \kappa_{p2})}{(\kappa_{p2} + (m-1)\kappa_{gf}) + \phi_{MT}(\kappa_{gf} - \kappa_{p2})} \right]; \frac{\kappa_{gf}}{\kappa_f} = \left[ \frac{(\kappa_{p1} + (m-1)\kappa_f) - (m-1)\phi_{ST}(\kappa_f - \kappa_{p1})}{(\kappa_{p1} + (m-1)\kappa_f) + \phi_{ST}\kappa_f - \kappa_{p1}} \right]$

**Table 2.** Thermo-physical features of hybrid nanofluids.

nanofluid and  $\phi_{hnf} = \phi_{ST} + \phi_{MT}$  is the nano solid particles magnitude measurement for the combination nano-fluid.  $\mu_f, \rho_f, (C_p)_f, \kappa_f$  and  $\sigma_f$  are functional viscidness, density, exact thermal capacity, and heat conductivity of the base fluid.  $\rho_{p1}, \rho_{p2}, (C_p)_{p1}, (C_p)_{p2}, \kappa_{p1}$  and  $\kappa_{p2}$  are the density, specific heat capacity, and thermal conductivity of the nano-molecules.

**Nano solid-particle shape-factor  $m$ .** The scale of the multiple nano solid-particles is defined as the shaped-nanoparticles factor. Table 3 shows the importance of the experiential form factor for different particle forms (for instance, see Xu and Chen<sup>73</sup>).

**Nano solid-particles and basefluid lineaments.** In this analysis, the material characteristics of the primary oil-based liquid of the engine are specified in Table 4<sup>74,75</sup>.

**Rosseland approximation.** Radiative flow only passes a shortened distance because its non-Newtonian P-EHNF is thicker. Because of this, the approximation for radiative fluxing from Rosseland<sup>76</sup> is utilised in formula (4).

$$q_r = -\frac{4\sigma^*}{3k^*} \frac{\partial \mathbb{Y}^4}{\partial y}, \tag{7}$$

herein,  $\sigma^*$  signifies the constant worth of Stefan–Boltzmann and  $k^*$  symbols the rate.

**Dimensionless formulations model**

Given the similarity technology that transforms the governing PDEs into ODEs, the BVP formulas (2)–(6) are modified. Familiarising stream function  $\psi$  in the formula<sup>75</sup>

$$B_1 = \frac{\partial \psi}{\partial y}, B_2 = -\frac{\partial \psi}{\partial x}. \tag{8}$$

The specified similarity quantities are

$$\Omega(x, y) = \sqrt{\frac{b}{v_f}} y, \quad \psi(x, y) = \sqrt{v_f b x f(\Omega)}, \quad \theta(\Omega) = \frac{\mathbb{Y} - \mathbb{Y}_\infty}{\mathbb{Y}_w - \mathbb{Y}_\infty}. \tag{9}$$

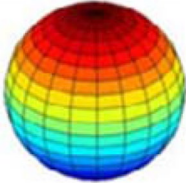


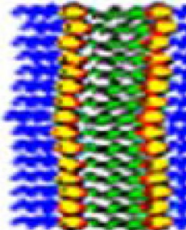

into Eqs. (2)–(4). We get

$$A_1^* f''' \left( 1 - A_2^* f'^2 \right) + \phi_b \left[ f f'' - f'^2 \right] - \frac{1}{\phi_a} K_\zeta f' = 0, \tag{10}$$

$$\theta'' \left( 1 + \frac{1}{\phi_d} P_\zeta N_\zeta \right) + P_\zeta \frac{\phi_c}{\phi_d} \left[ f \theta' - f' \theta + \frac{E_\zeta}{\phi_a \phi_c} f''^2 - \varepsilon_\zeta (f f' \theta' + f^2 \theta'') \right] = 0. \tag{11}$$

with



Nanoparticles type	Shape	Size (m)	Sphericity
Sphere		3	1.0
Hexahedron		3.7221	0.87
Tetrahedron		4.0613	0.82
Column		6.3698	0.61
Lamina		16.1576	0.33

**Table 3.** Shape-factor worth for different molecules shape.

Thermophysical	$\rho(\text{kg m}^{-3})$	$c_p(\text{J kg}^{-1} \text{K}^{-1})$	$k(\text{W mK}^{-1})$
SWCNTs	2600	425	6000
MWCNTs	1600	796	3000
Engine Oil (EO)	884	1910	0.144

**Table 4.** Fabricated materials thermo-physical attributes.

$$\left. \begin{aligned} f(0) = S, f'(0) = 1 + \Lambda_\zeta f''(0), \quad \theta'(0) = -H_\zeta(1 - \theta(0)) \\ f'(\Omega) \rightarrow 0, \theta(\Omega) \rightarrow 0, \quad \text{as } \Omega \rightarrow \infty. \end{aligned} \right\} \quad (12)$$

where  $\phi_i$ 's is  $a \leq i \leq d$  in formulas (10) and (11) signify the subsequent thermo-physical structures for P-HNF

$$\phi_a = (1 - \phi_{ST})^{2.5}(1 - \phi_{MT})^{2.5}, \quad \phi_b = (1 - \phi_{MT}) \left[ (1 - \phi_{ST}) + \phi_{ST} \frac{\rho_{p1}}{\rho_f} \right] + \phi_{MT} \frac{\rho_{p2}}{\rho_f}, \quad (13)$$

$$\phi_c = (1 - \phi_{MT}) \left\{ (1 - \phi_{ST}) + \phi_{ST} \frac{(\rho C_p)_{p1}}{(\rho C_p)_f} \right\} + \phi_{MT} \frac{(\rho C_p)_{p2}}{(\rho C_p)_f}, \quad (14)$$

$$\phi_d = \left[ \frac{(\kappa_{p_2} + (m - 1)\kappa_{nf}) - (m - 1)\phi_{MT}(\kappa_{nf} - \kappa_{p_2})}{(\kappa_{p_2} + (m - 1)\kappa_{nf}) + \phi_{MT}(\kappa_{nf} - \kappa_{p_2})} \right] \left[ \frac{(\kappa_{p_1} + (m - 1)\kappa_f) + \phi_{ST}(\kappa_f - \kappa_{p_1})}{(\kappa_{p_1} + (m - 1)\kappa_f) - (m - 1)\phi_{ST}(\kappa_f - \kappa_{p_1})} \right]. \tag{15}$$

**Explanation of the entrenched control constraints.** Equation (2) is accurately confirmed. Previously, the representation ' existed for demonstrating the derivatives regarding  $\Omega$ .

Symbols	Name	Formule	Default value
$A_1^*$	Prandtl–Eyring parameter-I	$A_1^* = \frac{A_d}{\mu_f}$	1.0
$A_2^*$	Prandtl–Eyring parameter-II	$A_2^* = \frac{b^*x^2}{2C^2v_f}$	0.4
$\varepsilon_\zeta$	Relaxation time parameter	$\varepsilon_\zeta = b\lambda_0$	0.2
$P_\zeta$	Prandtl number	$P_\zeta = \frac{v_f}{\alpha_f}$	6450
$\phi$	Volume fraction		0.18
$K_\zeta$	Porosity parameter	$K_\zeta = \frac{v_f}{bk}$	0.2
$S$	Suction/injection parameter	$S = -V_\zeta \sqrt{\frac{1}{v_f b}}$	0.4
$N_\zeta$	Thermal radiation parameter	$N_\zeta = \frac{16}{3} \frac{\sigma^* \mathbb{Y}_\infty^3}{\kappa^* v_f (\rho C_p)_f}$	0.3
$E_\zeta$	Eckert number	$E_\zeta = \frac{U_w^2}{(C_p)_f (\mathbb{Y}_w - \mathbb{Y}_\infty)}$	0.3
$H_\zeta$	Biot number	$H_\zeta = \frac{h_\zeta}{k_\zeta} \sqrt{\frac{v_f}{b}}$	0.3
$m$	Shape parameter (spherical)	$m$	3
$\Lambda_\zeta$	Velocity slip	$\Lambda_\zeta = \sqrt{\frac{b}{v_f}} N_\zeta$	0.3

**Drag-force and Nusselt number.** The drag-force ( $C_f$ ) combined with the Nusselt amount ( $Nu_x$ ) are the interesting physical amounts that controlled the flowing and specified as<sup>66</sup>

$$C_f = \frac{\tau_w}{\frac{1}{2}\rho_f U_w^2}, \quad Nu_x = \frac{xq_w}{k_f(\mathbb{Y}_w - \mathbb{Y}_\infty)} \tag{16}$$

where  $\tau_w$  and  $q_w$  determine as

$$\tau_w = \left( \frac{A_d}{C} \frac{\partial B_1}{\partial y} + \frac{A_d}{6C^3} \left( \frac{\partial B_1}{\partial y} \right)^3 \right)_{y=0}, \quad q_w = -k_{hmf} \left( 1 + \frac{16}{3} \frac{\sigma^* \mathbb{Y}_\infty^3}{\kappa^* v_f (\rho C_p)_f} \right) \left( \frac{\partial \mathbb{Y}}{\partial y} \right)_{y=0} \tag{17}$$

The dimensionless transmutations (9) are implemented to obtain

$$C_f Re_x^{\frac{1}{2}} = A_1^* f''(0) - \frac{1}{3} A_1^* A_2^* (f''(0))^3, \quad Nu_x Re_x^{-\frac{1}{2}} = -\frac{k_{hmf}}{k_f} (1 + N_\zeta) \theta'(0), \tag{18}$$

where  $Nu_x$  means Nusselt aggregate and  $C_f$  states drag force constant.  $Re_x = \frac{u_w x}{v_f}$  is local  $Re$  built in the extended swiftness  $u_w(x)$ .

### Classical Keller box technique

Because of its rapid convergence, the Keller-box approach (KBM)<sup>77</sup> is used to find solutions for model formulas (Fig. 2). KBM is used to find the localised solve of (10) and (11) with constraints (12). The policy of KBM is specified as next:

**Stage 1: ODEs adaptation.** In the early stage, all of the ODEs must be changed into 1st-order ODEs (10)–(12)

$$z_1 = f', \tag{19}$$

$$z_2 = z_1', \tag{20}$$

$$z_3 = \theta', \tag{21}$$

$$A_1^* z_2' (1 - A_2^* z_2^2) + \phi_b [fz_2 - z_1^2] - \frac{1}{\phi_a} K_\zeta z_1 = 0, \tag{22}$$



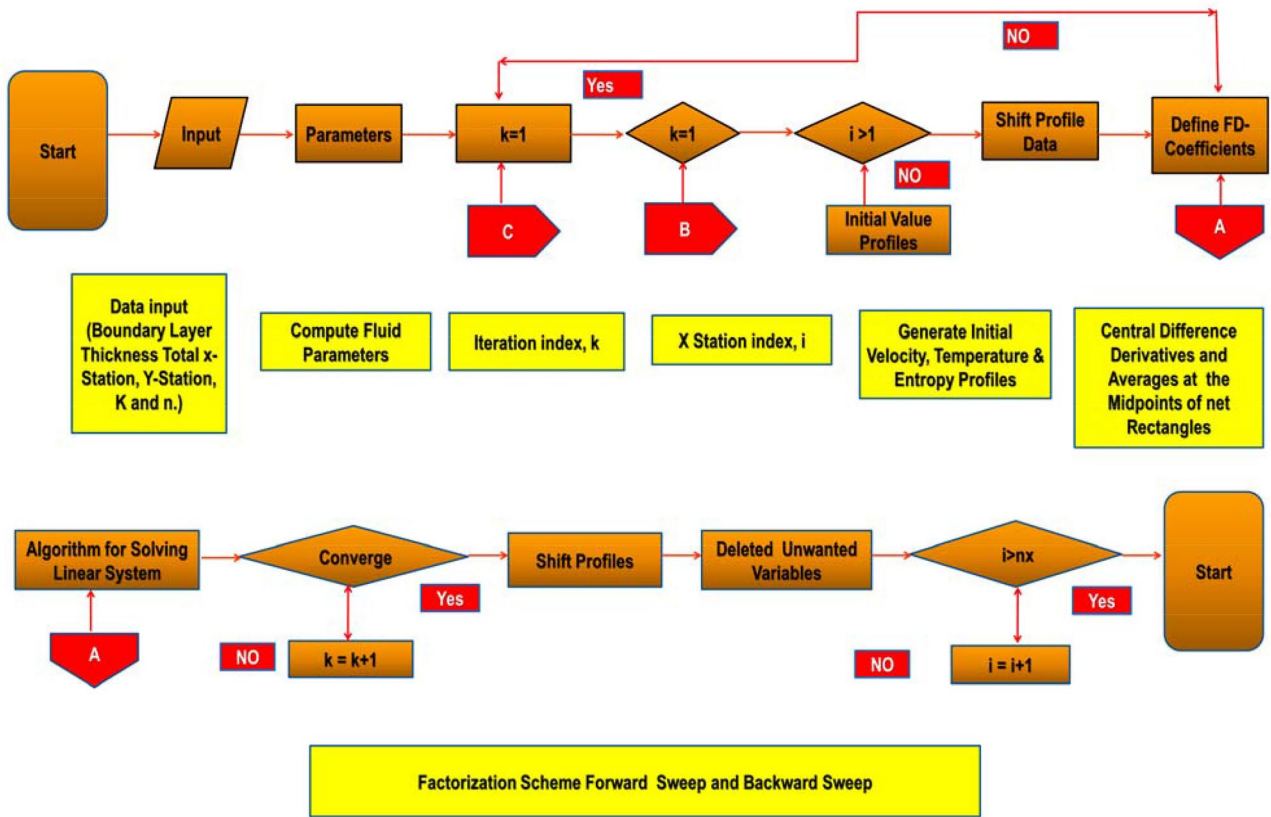


Figure 2. Chart of KBM steps.

$$z_3' \left( 1 + \frac{1}{\phi_d} P_\zeta N_\zeta \right) + P_\zeta \frac{\phi_c}{\phi_d} \left[ fz_3 - z_1 \theta + \frac{E_\zeta}{\phi_a \phi_c} z_2^2 - \varepsilon_\zeta (fz_1 z_3 + f^2 z_3') \right] = 0. \tag{23}$$

$$f(0) = S, z_1(0) = 1 + \Lambda_\zeta z_2(0), z_3(0) = -H_\zeta (1 - \theta(0)), z_1(\infty) \rightarrow 0, \theta(\infty) \rightarrow 0. \tag{24}$$

**Stage 2: separation of domains.** Discretisation plays a very important in the field of awareness. Discretising is usually conducted by making the area separated into equivalent-sized grids. Relatively lesser grids results are chosen in obtaining a higher precision for the calculation outcomes.

$$\Omega_0 = 0, \quad \Omega_j = \Omega_{j-1} + h, \quad j = 1, 2, 3, \dots, J - 1, \quad \Omega_J = \Omega_\infty.$$

where  $j$  is used for the spacing in  $h$  in a horizontal direction to show the position of the coordinates. The solution to the problem is to be found without any initial approximation. It is very crucial for finding velocity, temperatures, temperature variations, and entropy to make a preliminary assumption between  $\Omega = 0$  and  $\Omega = \infty$ . The frameworks from the result have been approximated solutions provided as they can happen the boundary conditions of the problem. It is imperative to remark that the results must be equal with different preliminary estimations are chosen, but the replication computation and time are varied which have been taken for conducting the calculations (see Fig. 3):

By implementing significant differences, difference equivalences are figured, and functions are used to replace the mean values. The 1st-order ODEs (19)–(23) have been modified to algebraic formulas which are non-linear.

$$\frac{(z_1)_j + (z_1)_{j-1}}{2} = \frac{f_j - f_{j-1}}{h}, \tag{25}$$

$$\frac{(z_2)_j + (z_2)_{j-1}}{2} = \frac{(z_1)_j - (z_1)_{j-1}}{h}, \tag{26}$$

$$\frac{(z_3)_j + (z_3)_{j-1}}{2} = \frac{\theta_j - \theta_{j-1}}{h}, \tag{27}$$

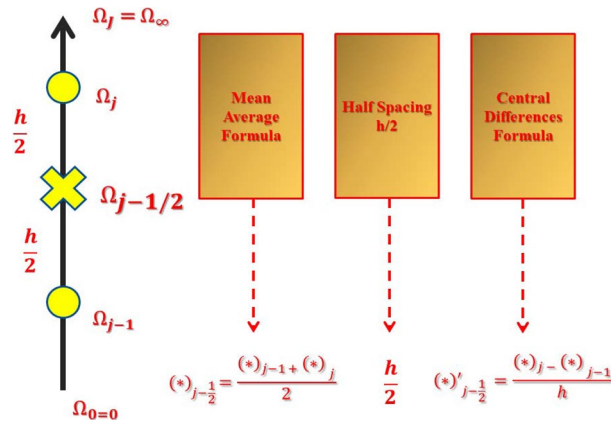


**Figure 3.** Net rectangle for showing difference approximations.

$$A_1^* \left( \frac{(z_2)_j - (z_2)_{j-1}}{h} \right) \left( 1 - A_2^* \left( \frac{(z_2)_j + (z_2)_{j-1}}{2} \right)^2 \right) + \left[ \phi_b \left( \left( \frac{f_j + f_{j-1}}{2} \right) \left( \frac{(z_2)_j + (z_2)_{j-1}}{2} \right) - \left( \frac{(z_1)_j + (z_1)_{j-1}}{2} \right)^2 \right) - K_\zeta \frac{1}{\phi_a} \left( \frac{(z_1)_j + (z_1)_{j-1}}{2} \right) \right], \tag{28}$$

$$\left( \frac{(z_3)_j - (z_3)_{j-1}}{h} \right) \left( 1 + \frac{1}{\phi_d} P_\zeta N_\zeta \right) + P_\zeta \frac{\phi_c}{\phi_d} \left[ \left( \frac{f_j + f_{j-1}}{2} \right) \left( \frac{(z_3)_j + (z_3)_{j-1}}{2} \right) \right] + Pr \frac{\phi_c}{\phi_d} \left[ \frac{E_\zeta}{\phi_a \phi_c} \left( \frac{(z_2)_j + (z_2)_{j-1}}{2} \right)^2 - \left( \frac{(z_1)_j + (z_1)_{j-1}}{2} \right) \left( \frac{\theta_j + \theta_{j-1}}{2} \right) \right] - Pr \frac{\phi_c}{\phi_d} \left[ \varepsilon_\zeta \left( \left( \frac{f_j + f_{j-1}}{2} \right) \left( \frac{(z_1)_j + (z_1)_{j-1}}{2} \right) \left( \frac{(z_3)_j + (z_3)_{j-1}}{2} \right) + \left( \frac{f_j + f_{j-1}}{2} \right)^2 \left( \frac{(z_3)_j - (z_3)_{j-1}}{h} \right) \right) \right] = 0. \tag{29}$$

**Stage 3: linearisation based on Newton’s method.** The resulting formulas have been completed linearly by using Newton’s process.  $(i + 1)^{th}$  iterations can be found in the earlier equations

$$()^{(i+1)} = ()^{(i)} + \ddot{\theta}()^{(i)}. \tag{30}$$

By replacing this in (25) to (29) and after overlooking the higher-elevated bounds of  $\ddot{\theta}^i$  a linear tri-diagonal equation scheme has been resulting as follows:

$$\ddot{\theta}f_j - \ddot{\theta}f_{j-1} - \frac{1}{2}h(\ddot{\theta}(z_1)_j + \ddot{\theta}(z_1)_{j-1}) = (r_1)_{j-\frac{1}{2}}, \tag{31}$$

$$\ddot{\theta}(z_1)_j - \ddot{\theta}(z_1)_{j-1} - \frac{1}{2}h(\ddot{\theta}(z_2)_j + \ddot{\theta}(z_2)_{j-1}) = (r_2)_{j-\frac{1}{2}}, \tag{32}$$

$$\ddot{\theta}\theta_j - \ddot{\theta}\theta_{j-1} - \frac{1}{2}h(\ddot{\theta}(z_3)_j + \ddot{\theta}(z_3)_{j-1}) = (r_3)_{j-\frac{1}{2}}, \tag{33}$$

$$(a_1)_j \ddot{\theta}f_j + (a_2)_j \ddot{\theta}f_{j-1} + (a_3)_j \ddot{\theta}z_1_j + (a_4)_j \ddot{\theta}z_1_{j-1} + (a_5)_j \ddot{\theta}z_2_j + (a_6)_j \ddot{\theta}z_2_{j-1} + (a_7)_j \ddot{\theta}\theta_j + (a_8)_j \ddot{\theta}\theta_{j-1} + (a_9)_j \ddot{\theta}(z_3)_j + (a_{10})_j \ddot{\theta}(z_3)_{j-1} = (r_4)_{j-\frac{1}{2}}, \tag{34}$$

$$(b_1)_j \ddot{\theta}f_j + (b_2)_j \ddot{\theta}f_{j-1} + (b_3)_j \ddot{\theta}z_1_j + (b_4)_j \ddot{\theta}z_1_{j-1} + (b_5)_j \ddot{\theta}z_2_j + (b_6)_j \ddot{\theta}z_2_{j-1} + (b_7)_j \ddot{\theta}\theta_j + (b_8)_j \ddot{\theta}\theta_{j-1} + (b_9)_j \ddot{\theta}(z_3)_j + (b_{10})_j \ddot{\theta}(z_3)_{j-1} = (r_5)_{j-\frac{1}{2}}. \tag{35}$$

where

$$(r_1)_{j-\frac{1}{2}} = -f_j + f_{j-1} + \frac{h}{2}(z_1)_j + ((z_1)_{j-1}), \tag{36}$$



$Pr$	Ref. <sup>78</sup>	Ref. <sup>79</sup>	Present
$72 \times 10^{-2}$	$080863135 \times 10^{-8}$	$080876122 \times 10^{-8}$	$080876181 \times 10^{-8}$
$1 \times 10^0$	$1 \times 10^0$	$1 \times 10^0$	$1 \times 10^0$
$3 \times 10^0$	$192,368,259 \times 10^{-8}$	$192,357,431 \times 10^{-8}$	$192,357,420 \times 10^{-8}$
$7 \times 10^0$	$307,225,021 \times 10^{-8}$	$307,314,679 \times 10^{-8}$	$307,314,651 \times 10^{-8}$
$10 \times 10^0$	$372,067,390 \times 10^{-8}$	$372,055,436 \times 10^{-8}$	$372,055,429 \times 10^{-8}$

**Table 5.** Comparing of  $-\theta'(0)$  values with  $P_\zeta$ , when  $\phi = 0, \phi_{mf} = 0, \varepsilon_\zeta = 0, \Lambda_\zeta = 0, E_\zeta = 0, N_\zeta = 0, S = 0$  and  $H_\zeta \rightarrow \infty$ .

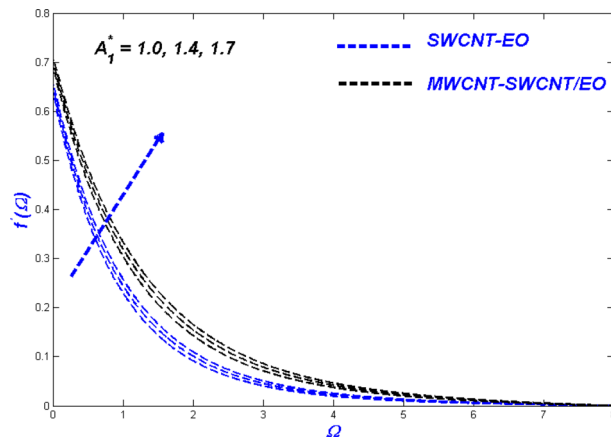


**Figure 4.** Velocity change with  $A_1^*$ .

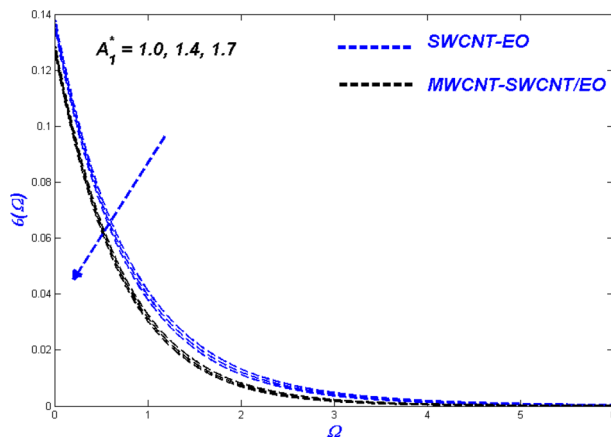


**Figure 5.** Temperature change with  $A_1^*$ .

By formula (9), the non-dimensional entropy formula is:

$$N_G = Re \left[ \phi_d (1 + N_\zeta) \theta'^2 + \frac{1}{\phi_a} \frac{B_\zeta}{\Pi} (f''^2 + H_\zeta f'^2) \right], \tag{46}$$

Here  $Re$  is the Reynolds number,  $B_\zeta$  signifies Brinkmann amount and  $\Pi$  symbols the non-dimensional variation of the temperature.

### Results and discussion

An adequate discussion is indicated by numerical results that reach the model described before. As a result of these potential parameters, the values for  $A_1^*, A_2^*, K_\zeta, \phi, \Lambda_\zeta, S, N_\zeta, \varepsilon_\zeta, E_\zeta, H_\zeta, Re$  and  $B_\zeta$  been illustrated. These parameters show the physical performance of the non-dimensional quantities in Figs. 4, 5, 6, 7, 8, 9, 10, 11, 12,

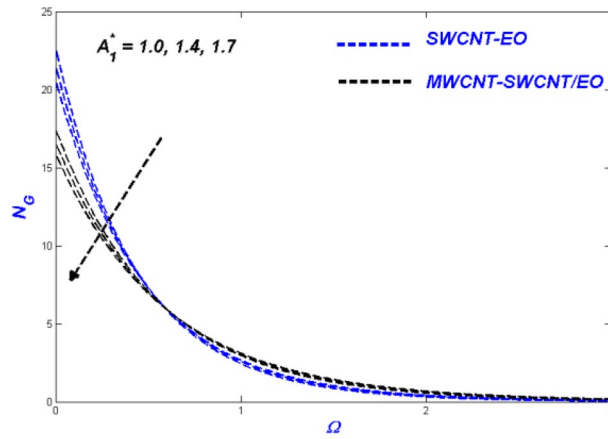


**Figure 6.** Entropy change with  $A_1^*$ .

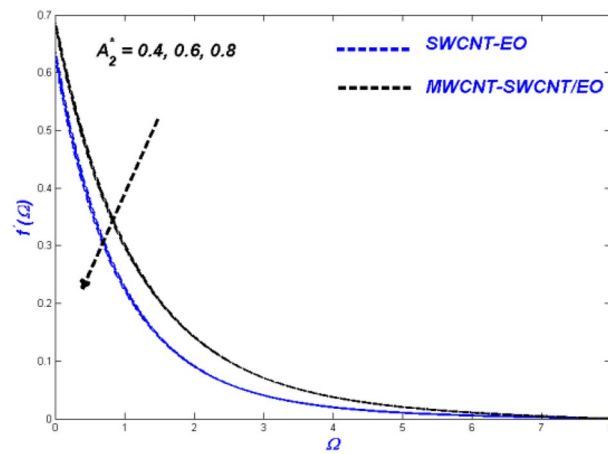


**Figure 7.** Velocity change with  $A_2^*$ .

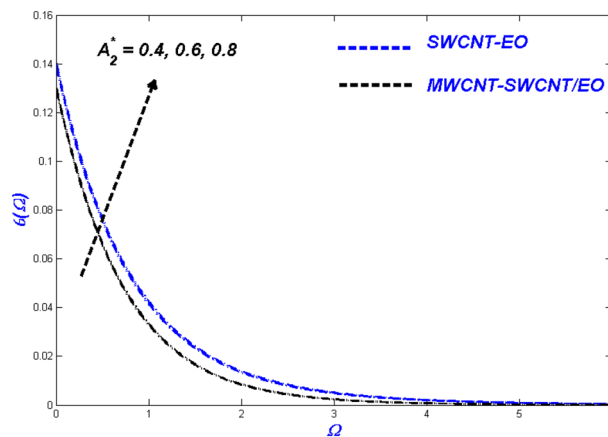


**Figure 8.** Temperature change with  $A_2^*$ .

13, 14, 15, 16, 17, 18, 19, 20, 21, 22, 23, 24, 25 and 26, such as velocity, energy, and entropy production. The results are obtained for Cu-EO normal P-ENF and MWCNT-SWCNT/EO non-Newtonian P-EHNF. The coefficient of skin friction and temperature variations are shown in Table 6. For example, the default values were 1.0 for  $A_1^*$  and 0.4 for  $A_2^*$ ,  $K_\zeta$  was set to be equal to 0.1, and  $\phi = 0.18$ ,  $\phi_{MT}$  was set to 0.09,  $\Lambda_\zeta$  was set to 0.3,  $S$  was set to 0.4, and  $N_\zeta$  was set to 0.3,  $\varepsilon_\zeta$  was set to 0.1,  $E_\zeta$  was set to 0.3,  $H_\zeta$  was set to 0.3, and  $R_c$  and  $B_c$  was set to 5.

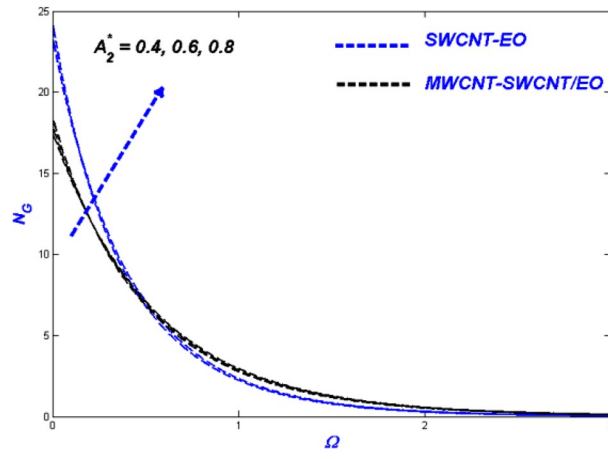


Figure 9. Entropy change with  $A_2^*$ .

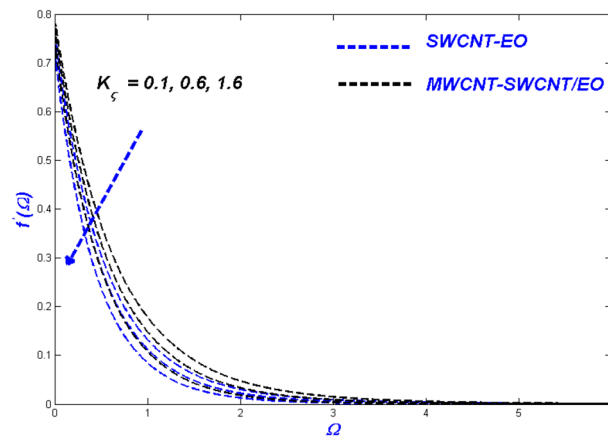


Figure 10. Velocity change with  $K_ζ$ .

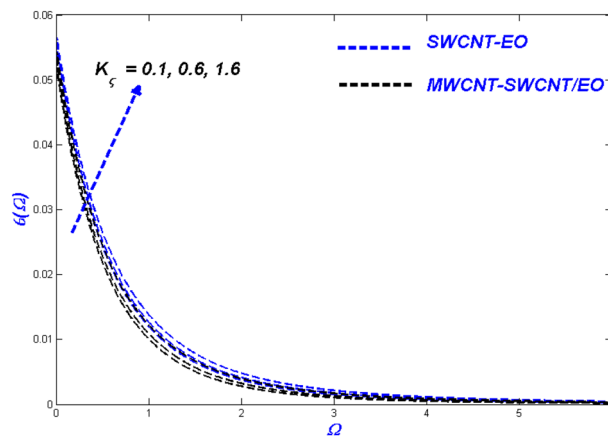


Figure 11. Temperature change with  $K_ζ$ .

**Influence of Prandtl–Eyring parameter  $A_1^*$ .** Figures 4, 5 and 6 illustrate the influence of the Prandtl–Eyring parameter  $A_1^*$  on the velocity, energy, and entropy distributions of the Prandtl–Eyring hybrid nanofluid, respectively.  $A_1^*$ 's velocity fluctuation ( $f'$ ) is seen in Fig. 4. As the value of  $A_1^*$  was elevated, so was the velocity profile for both fluids. The physical reason for this occurrence is that it causes the fluid's viscosity to decrease, reducing resistance while boosting fluid velocity. MWCNT-SWCNT nanofluid, on the other hand, has faster



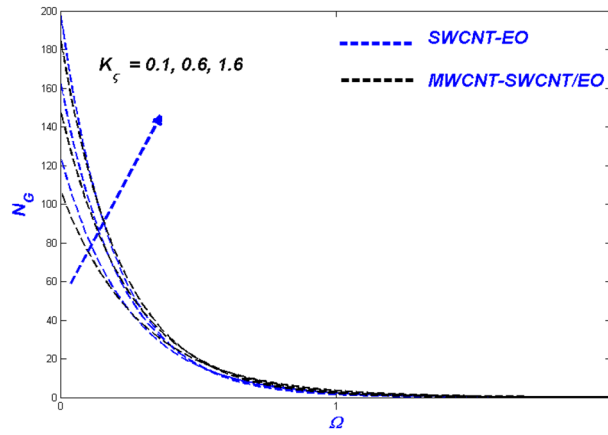


Figure 12. Entropy change with  $K_\zeta$ .

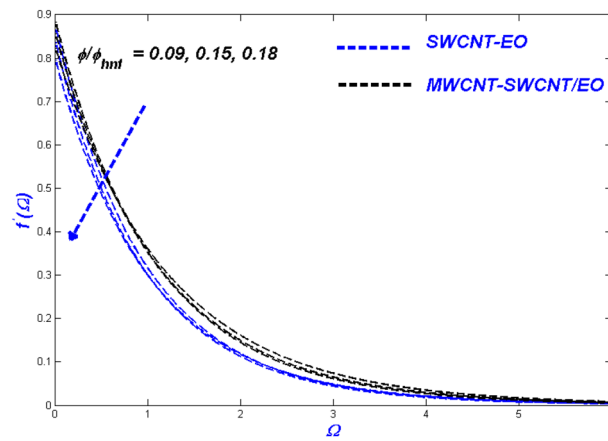


Figure 13. Velocity change with  $\phi/\phi_{hmf}$ .

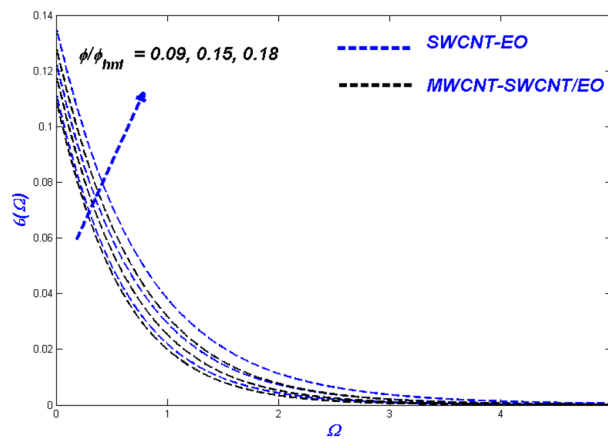


Figure 14. Temperature change with  $\phi/\phi_{hmf}$ .

acceleration than SWCNT nanofluid. It can be explained as the hybrid nanofluid have an enormous density impact rather than the nanofluid. The temperature curve for the Prandtl–Eyring parameter  $A_1^*$  is shown in Fig. 5. MWCNT-SWCNT hybrid nanofluid had a lower temperature profile since the value of  $A_1^*$  was raised, while the Cu nanofluid had a higher temperature profile. More heat can be conveyed faster when the caused in this lowered manner due to velocity improve and expand. Another important distinction is that the hybrid nanofluid

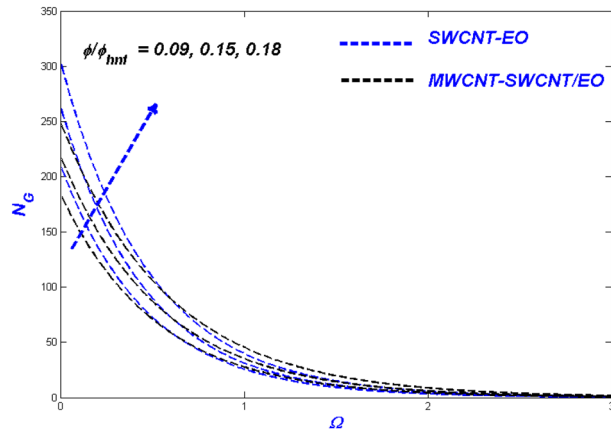


Figure 15. Entropy change with  $\phi/\phi_{hmf}$ .

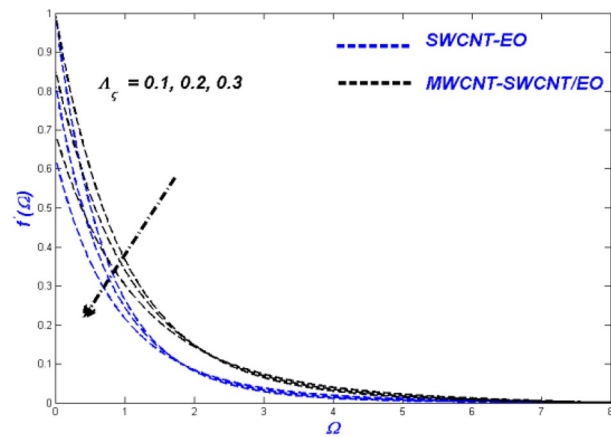


Figure 16. Velocity change with  $\Lambda_{\zeta}$ .

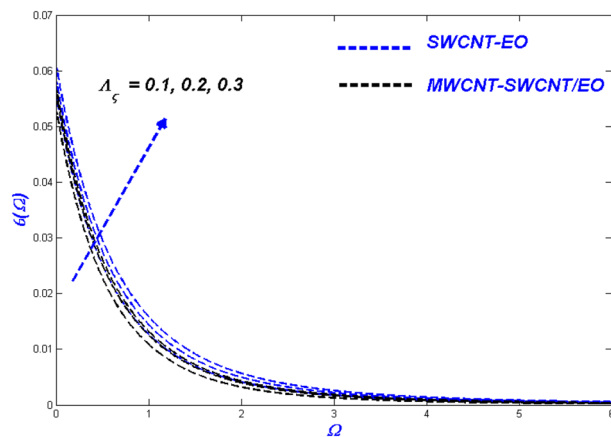


Figure 17. Temperature change with  $\Lambda_{\zeta}$ .

exhibits significantly reduced thermal conductivity when compared to pure nanofluid. Figure 6 depicted the Prandtl–Eyring hybrid nanofluid entropy fluctuation based on its parameter  $A_1^*$ . The quantity of entropy produced decreased as the amount of  $A_1^*$  enhanced. MWCNT-SWCNT fluid exhibited a lower entropy value than SWCNT hybrid nanofluid, even though their values were the same at one point in the graph. This phenomenon

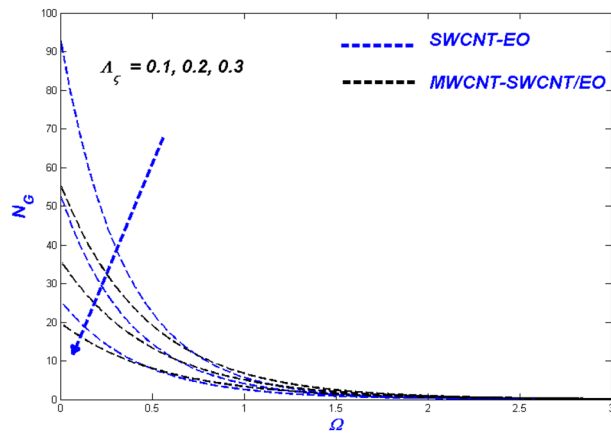


Figure 18. Entropy change with  $\Lambda_\zeta$ .

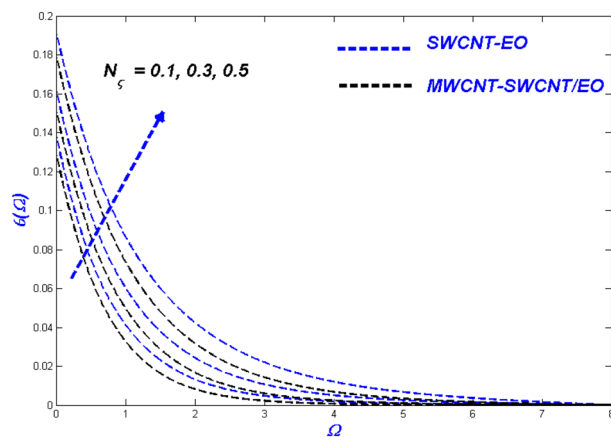


Figure 19. Temperature change with  $N_\zeta$ .

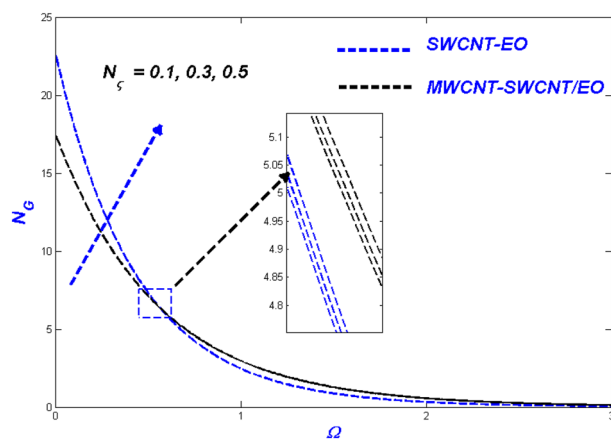


Figure 20. Entropy change with  $N_\zeta$ .

occurs due to the low temperatures reducing hybrid nanofluid mobility, causing the system's entropy to proliferation.

**Influence of Prandtl–Eyring parameter  $A_2^*$ .** There was an influence of Prandtl–Eyring Parameter  $A_2^*$  on the Prandtl–Eyring hybrid nanofluid temperature, velocity, and entropy production profile (see Figs. 7, 8). Fig-

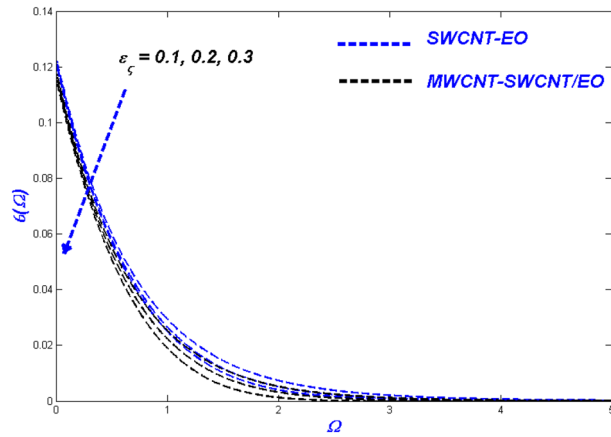


Figure 21. Temperature change with  $\varepsilon_\zeta$ .

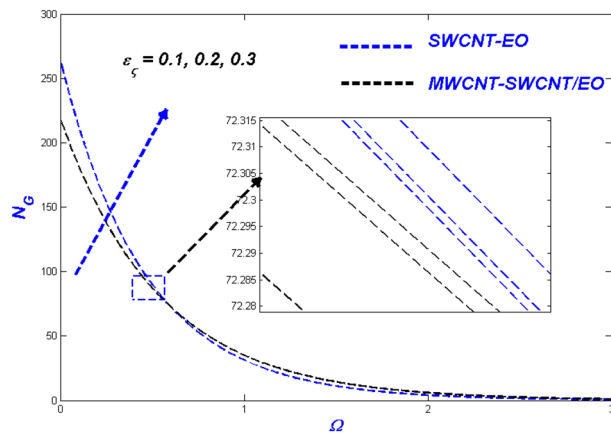


Figure 22. Entropy change with  $\varepsilon_\zeta$ .

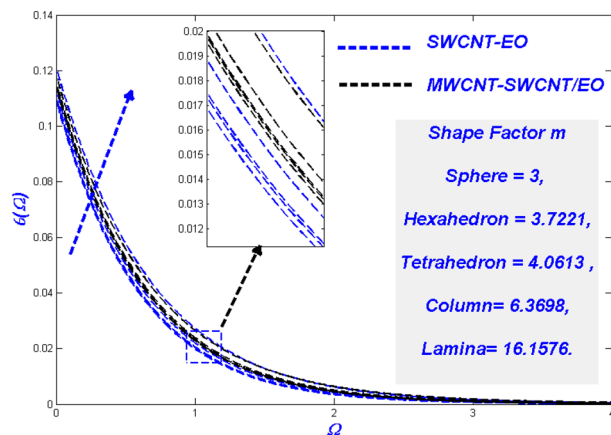


Figure 23. Temperature change with  $m$ .

ure 7 depicts the varying  $A_2^*$  with velocity. The velocity profile narrows as  $A_2^*$  rises, with MWCNT-SWCNT/EO achieving a higher top speed than SWCNT-EO. Hybrid nanofluid particles have resistance due to the fact that they vary inversely with momentum diffusivity. As a result, the flow's velocity will be reduced with  $A_2^*$ . This phenomenon is because SWCNT-EO has a higher density and hence has a thicker flow than MWCNT-SWCNT/EO, making the fluid challenging to transport. Figure 8 shows the temperature change after  $A_2^*$  has had its impact. As

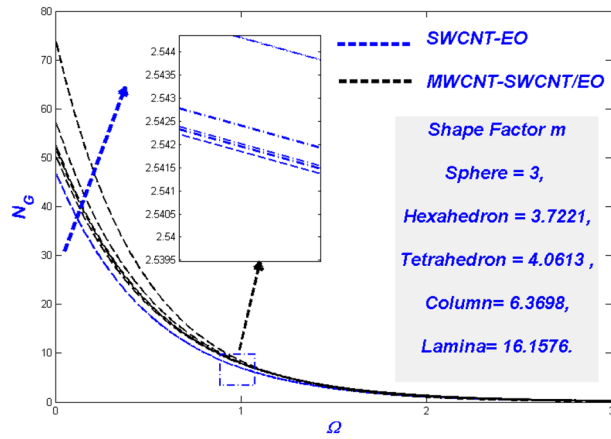


Figure 24. Entropy change with  $m$ .

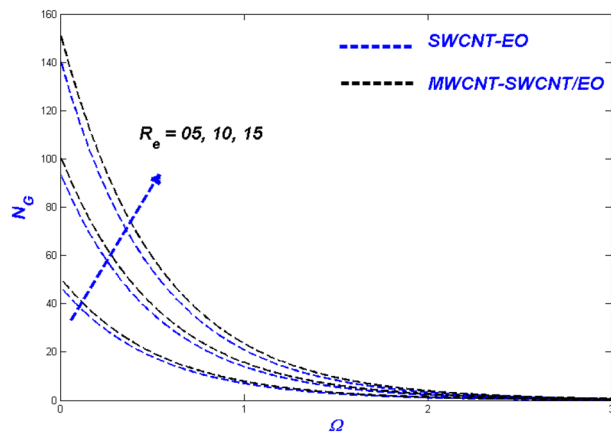


Figure 25. Entropy change with  $R_e$ .

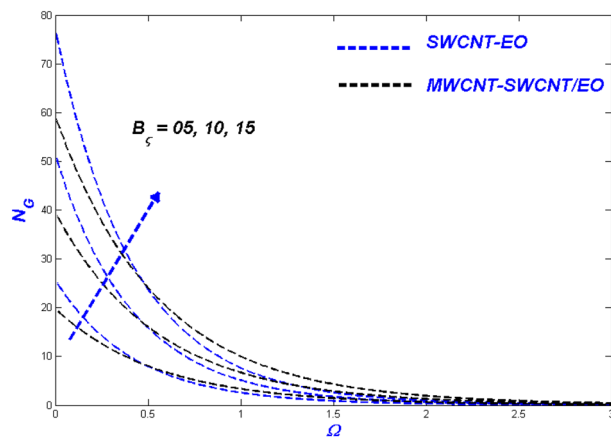


Figure 26. Entropy change with  $B_ζ$ .

the value of  $A_2^*$  grew, so did the temperature, with SWCNT-EO quickly reaching the desired temperature. The occurrence happens because the flow velocity dropped, and as a result, the heat transmission from the surface was degraded. Figure 9 shows the change in entropy according to the Prandtl–Eyring parameter  $A_2^*$ . The entropy profile grew as the value of  $A_2^*$  grew, showing a clear connection between the two. It suggested that  $A_2^*$  amplifying the impediment in the system, resulting in the entropy of the developing system being elevated.

$A_1^*$	$A_2^*$	$K_\zeta$	$\phi$	$\phi_{MT}$	$\Lambda_\zeta$	$S$	$N_\zeta$	$\epsilon_\zeta$	$H_\zeta$	$C_f Re_x^{1/2}$ SWCNT-EO	$C_f Re_x^{1/2}$ MWCNT-SWCNT/EO	$Nu_x Re_x^{-1/2}$ SWCNT-EO	$Nu_x Re_x^{-1/2}$ MWCNT-SWCNT/EO
1.0	0.4	0.1	0.18	0.09	0.3	0.4	0.3	0.2	0.3	4.7980	5.4521	2.5615	3.0496
1.4										4.8262	5.4884	2.5974	3.0727
1.7										4.8561	5.5173	2.6299	3.1092
	0.4									4.7980	5.4521	2.5615	3.0496
	0.6									4.7629	5.4264	2.5426	3.0138
	0.8									4.7487	5.3933	2.5273	3.0095
		0.1								4.7980	5.4521	2.5615	3.0496
		0.6								4.8113	5.4816	2.5381	3.0230
		1.6								4.8335	5.5250	2.5045	3.0045
			0.09							4.7372	–	2.5126	–
			0.15							4.7543	–	2.5458	–
			0.18							4.7980	–	2.5615	–
				0.0						–	4.7372	–	2.5126
				0.06						–	5.4377	–	3.0123
				0.09						–	5.4521	–	3.0496
					0.1					4.8626	5.5143	2.6083	3.0911
					0.2					4.8397	5.4916	2.5851	3.0648
					0.3					4.7980	5.4521	2.5615	3.0496
						0.2				4.7647	5.4305	2.5229	3.0092
						0.4				4.7980	5.4521	2.5615	3.0496
						0.6				4.8131	5.4845	2.5882	3.0675
							0.1			4.7980	5.4521	2.5237	3.0282
							0.3			4.7980	5.4521	2.5615	3.0496
							0.5			4.7980	5.4521	2.5925	3.0755
								0.1		4.7980	5.4521	2.5949	3.0754
								0.2		4.7980	5.4521	2.5615	3.0496
								0.3		4.7980	5.4521	2.5337	3.0042
									0.1	4.7980	5.4521	2.5359	3.0148
									0.3	4.7980	5.4521	2.5615	3.0496
									0.5	4.7980	5.4521	2.5979	3.0636

**Table 6.** Values of  $C_f Re_x^{1/2}$  and  $Nu_x Re_x^{-1/2}$  for  $P_\zeta = 6450$ .

**Effect of porous media variable  $K_\zeta$ .** Figures 10, 11 and 12 demonstrate that surface porosity affects several outputs, including flow speed, domain heat, and entropy generation. Improving the variable ( $K_\zeta$ ) in Fig. 10 makes the surface more porous, allowing more fluid to flow through it. Due to the other particles, the hybrid nanofluid moves more slowly through the porous surface when compared to MWCNT-SWCNT/EO Prandtl–Eyring nanofluid. This occurrence might be because the added particles delay the hybrid nanofluid's flow through the porous surface. Figure 11 displays the expansion of the porous medium variable ( $K_\zeta$ ) results in better heat dispersion throughout the domain. When a hole is made in a porous medium, the flow slows down, allowing more time to collect heat from the surface. This phenomenon improves the thermal distribution around the area. Since particle motions across porous media are sluggish, the porosity aids in the irreversibility of energy transfer across the domain during entropy production ( $N_G$ ) (Fig. 12).

**Effect of nanomolecules size  $\phi$  and  $\phi_{hnf}$ .** The efficacy of the nanofluid and hybrid versions appears to be determined by the fractional nanoparticle size in the base fluid. The more excellent fractional range of nanoparticles reduces flowability because of the additional load it adds. For some reason, the fractional upgrade prefers the hybrid nanofluid over the single-nanofluid, which flows lower in Fig. 13. This incidence displayed the primary reason for utilising nano- and hybrid-based fluid mixtures because of their exceptional heat transmission properties. This degradation occurs as a result of excessive nanoparticle surface area and higher hybrid nanofluid density. As the fractional volume of both kinds of flow fluids improved, so did the resultant thermal distribution, as shown in Fig. 14. Because of the temperature difference, when the nano molecule size is reduced, the molecules will disperse in the far-field flow. The thermal boundary layer's thickness will rise as a result of this change. The minimal size of nano molecules can be utilised to create the lowest possible temperature profile, as determined through experimentation. Figure 15 exhibits the leading nanofluid varies in the middle and settles down to the hybrid nanofluid at the far end, with energy entropy fluctuations also intensifying for fractional volume. SWCNT-EO has a greater entropy than MWCNT-SWCNT/EO because the hybrid nanofluid has a far higher thermal conductivity than nanofluid.



**Effect of velocity slip variable  $\Lambda_\zeta$ .** Figures 16, 17 and 18 evaluate the impact of enhanced slip circumstances on flow nature, thermal features, and entropy forms. Figure 16 illustrates the flow conditions in Prandtl–Eyring fluid mixtures are primarily centred upon the viscous behaviour. Due to this occurrence, slip conditions become incredibly critical in fluids as a whole. For a hybrid suspended Prandtl–Eyring nanofluid, the viscous nature and higher levels of flow slip generate more complex fluidity circumstances, with the result that the fluidity of the single nanofluid drops even more rapidly. Due to the flow hierarchy, the SWCNT–EO nanofluid maintains a higher temperature state than the MWCNT–SWCNT/EO hybrid nanofluid, which is depicted in Fig. 17. The improvement in boundary layer viscosity due to the decline in velocity will have a similar effect. As a result, it will have skyrocketed the flow's temperature. Because the hybrid nanofluid has less viscosity than the conventional nanofluid, it is predicted MWCNT–SWCNT/EO to have a lower temperature than SWCNT–EO. A descending trend in entropy formation can be seen for higher slip parameters because the slipped flow acts against the domain's entropy formation.

**Thermal radiative variable  $N_\zeta$  and relaxation time parameter ( $\varepsilon_\zeta$ ) influence.** Figures 19 and 20 highlights the actual status of thermal diffusion and entropy generation under enhanced heat radiative flow limitation ( $N_\zeta$ ). Thermally diffusing nanofluids have a propensity to rise in temperature past the interesting domain, boosting the heat transmission burden for radiation constrictions on the transient nanofluid. This temperature rise may be explained in a physical sense by supposing that thermal radiation is converted into electromagnetic energy. As a result, the distance from the surface from which radiation is emitted rises, ultimately superheating the boundary layer flow. As a result, the thermal radiative variable is critical in determining the system's temperature profile. A limit on radiative flow ( $N_\zeta$ ) via entropy generation is illustrated in Fig. 20 by the overfilled dispersions. For different ( $N_\zeta$ ) values, the entropic side-by-side leans toward developing more in MWCNT–SWCNT/EO than in SWCNT–EO nanofluid. A reasonable explanation for this occurrence is the system's irreparable heat transfer mechanism is entirely irreversible. According to Fig. 21, greater values of the relaxation time parameter cause a rise in the temperature of the Tangent hyperbolic hybrid nanofluids, as seen in the graph. As the temperature drops, the thickness of the thermal boundary layer reduces. Table 5 shows that when the rate of heat output efficiency, the effectiveness of the thermal system improves as well. Figure 22 shows the impact of engine oil-based nanofluid entropy profiles. The velocity profile, on the other hand, shows no change, while the entropy of the system increases with varying values  $\varepsilon_\zeta$ .

**Effect of the diverse solid particle shape  $m$ .** It is well-known that NPs have high thermal conductivity and transfer rates under a variety of physical conditions. In porous medium difficulties, such nano-level particles become an issue, modelled using the shape variable ( $m$ ) in this study. From spherical ( $m = 3$ ) to lamina ( $m = 16.176$ ), the forms considered here ranged. To improve the thermal state, Fig. 23 indicates that nanoparticle shapes impact it. In comparison to SWCNT–EO mono nanofluid, the MWCNT–SWCNT/EO hybrid nanofluid has a more significant form impact. Hybrid nanofluid has a broader thermal layer boundary and a more excellent thermal distribution than nanofluid. Even in the MWCNT–SWCNT/EO hybrid nanofluid, the lamina ( $m = 16.176$ ) shaped particles remain ahead of the others. The main physical reason for this phenomenon is the lamina shape particles has the most remarkable viscosity while the sphere has the minimum viscosity. It is also noted that at a higher temperature, the viscosity of the particles will be diminished. This phenomenon happens because of the temperature-dependent shear-thinning characteristic. The profiles in Fig. 24 indicate the form factors have a more substantial influence in MWCNT–SWCNT/EO NHF, which has a higher entropy rate than SWCNT–EO mono nanofluid, even though the morphologies of the particles have a much less impact.

**Entropy variations for Reynolds number ( $R_e$ ) and Brinkman number ( $B_\zeta$ ).** Figure 25 depicted as Reynolds number proliferations ( $R_e$ ), the entropy rate ( $N_G$ ) improves as well. An aggregate Reynolds number supports nanoparticle mobility in porous media because of the dominance of inertial over viscous forces in the system. Consequently, entropy can be generated over the domain. MWCNT–SWCNT/EO HNF generated a higher entropy rate than MWCNT–SWCNT/EO nanofluid because of the combined efficiency of the particles. The Brinkman number ( $B_\zeta$ ) was used to describe the heat created by viscous properties because it enhances the generated heat above and beyond other thermal inputs. The heightened heat-inducing ability of such viscosity enhancement promotes entropy production in the system as a whole ( $N_G$ ). Figure 26 illustrated the elevated entropy layers, which improved the Brinkman number ( $B_\zeta$ ) values. The primary feature of viscous dislocation heat produces a decrease in the escalating Brinkman numbers, which theoretically leads to a higher rate of entropy development.

## Final results and future guidance

The entropy production and heat transmission by a Prandtl–Eyring hybrid nanofluid (P-EHNF) over a stretched sheet is studied. By utilising a single model phase, a computational model may be developed. Several physical characteristics are used to derive the results. These include changes in velocity, energy, and entropy. Cattaneo–Christov heat flux  $\varepsilon_\zeta$  is also discussed in this study, as are the effects of Prandtl–Eyring parameters  $A_1^*$  and  $A_2^*$  as well as  $K_\zeta$  for porous medium, nanomolecular size  $\phi$  and  $\phi_{hmf}$ ,  $\Lambda_\zeta$  for velocity slip, thermal radiative variable  $N_\zeta$  and Biot number  $H_\zeta$  as well as various solid particle shapes  $m$ ,  $R_e$  and  $B_\zeta$ . The following are the study's significant findings:

1. In comparison to traditional Prandtl–Eyring nanofluid (SWCNT/–EO), hybrid Prandtl–Eyring nanofluid (MWCNT–SWCNT/EO) is shown to be a superior thermal conductor.

2. Swelling the size of EO's nano solid particles can increase the rate of heat transmission.
3. Upsurges in the porous media variable  $K$ , the size parameters  $\phi$  and  $\phi_{hmf}$ , thermal radiative flow ( $N_\zeta$ ), the Brinkman number ( $B_\zeta$ ) and the Reynolds number ( $R_e$ ) growth the system's entropy, whereas the increase in the velocity slip parameter ( $\Lambda_\zeta$ ) reduces it.
4. Porous media variable increments enhance the velocity magnitude, whereas nano molecule swelling causes the speed to drop.

The current study's findings may help lead future heating system upgrades that evaluate the heating system's heat effect using a variety of non-Newtonian hybrid nanofluids (i.e., second-grade, Carreau, Casson, Maxwell, micropolar nanofluids, etc.). It's possible to depict the effects of temperature-dependent viscosity, temperature-dependent porosity, and magneto-slip flow by significantly expanding the scheme's capabilities.

Received: 3 September 2021; Accepted: 22 November 2021

Published online: 07 December 2021

## References

1. Aziz, T., Fatima, A., Khaliq, C. M. & Mahomed, F. M. Prandtl's boundary layer equation for two-dimensional flow: Exact solutions via the simplest equation method. *Math. Probl. Eng.* **2013**, 724385 (2013).
2. Sankad, G., Ishwar, M. & Dhange, M. Varying wall temperature and thermal radiation effects on MHD boundary layer liquid flow containing gyrotactic microorganisms. *Partial Differ. Equ. Appl. Math.* **4**, 100092 (2021).
3. Hussain, M. *et al.* MHD thermal boundary layer flow of a Casson fluid over a penetrable stretching wedge in the existence of non-linear radiation and convective boundary condition. *Alex. Eng. J.* **60**(6), 5473–5483 (2021).
4. Abedi, H., Sarkar, S. & Johansson, H. Numerical modelling of neutral atmospheric boundary layer flow through heterogeneous forest canopies in complex terrain (a case study of a Swedish wind farm). *Renew. Energy* **180**, 806–828 (2021).
5. Yang, S., Liu, L., Long, Z. & Feng, L. Unsteady natural convection boundary layer flow and heat transfer past a vertical flat plate with novel constitution models. *Appl. Math. Lett.* **120**, 107335 (2021).
6. Long, Z., Liu, L., Yang, S., Feng, L. & Zheng, L. Analysis of Marangoni boundary layer flow and heat transfer with novel constitution relationships. *Int. Commun. Heat Mass Transf.* **127**, 105523 (2021).
7. Hanif, H. A computational approach for boundary layer flow and heat transfer of fractional Maxwell fluid. *Math. Comput. Simul.* **191**, 1–13 (2022).
8. Ali, A., Awais, M., Al-Zubaidi, A., Saleem, S. & Marwat, D. N. K. Hartmann boundary layer in peristaltic flow for viscoelastic fluid: Existence. *Ain Shams Eng. J.* (2021) (in press). <https://doi.org/10.1016/j.asej.2021.08.001>
9. Suresh, S., Venkataraj, K. P., Selvakumar, P. & Chandrasekar, M. Synthesis of Al<sub>2</sub>O<sub>3</sub>-Cu/water hybrid nanofluids using two step method and its thermo physical properties. *Colloid Surf. A Physicochem. Eng. Asp.* **388**, 41–48 (2021).
10. Yildiz, C., Arici, M. & Karabay, H. Comparison of a theoretical and experimental thermal conductivity model on the heat transfer performance of Al<sub>2</sub>O<sub>3</sub>-SiO<sub>2</sub>/water hybrid-nanofluid. *Int. J. Heat Mass Transf.* **140**, 598–605 (2019).
11. Waini, I., Ishak, A. & Pop, I. Flow and heat transfer along a permeable stretching/shrinking curved surface in a hybrid nanofluid. *Phys. Scr.* **94**(10), 105219 (2019).
12. Qureshi, M. A., Hussain, S. & Sadiq, M. A. Numerical simulations of MHD mixed convection of hybrid nanofluid flow in a horizontal channel with cavity: Impact on heat transfer and hydrodynamic forces. *Case Stud. Therm. Eng.* **27**, 101321 (2021).
13. Mabood, F. & Akinshilo, A. T. Stability analysis and heat transfer of hybrid Cu-Al<sub>2</sub>O<sub>3</sub>/H<sub>2</sub>O nanofluids transport over a stretching surface. *Int. Commun. Heat Mass Transf.* **123**, 105215 (2021).
14. Zhang, Y., Shahmir, N., Ramzan, M., Alotaibi, H. & Aljohani, H. M. Upshot of melting heat transfer in a Von Karman rotating flow of gold-silver/engine oil hybrid nanofluid with Cattaneo-Christov heat flux. *Case Stud. Therm. Eng.* **26**, 101149 (2021).
15. Arif, M., Kumam, P., Khan, D. & Wathayay, W. Thermal performance of GO-MoS<sub>2</sub>/engine oil as Maxwell hybrid nanofluid flow with heat transfer in oscillating vertical cylinder. *Case Stud. Therm. Eng.* **27**, 101290 (2021).
16. Vinoth, R. & Sachuthananthan, B. Flow and heat transfer behavior of hybrid nanofluid through microchannel with two different channels. *Int. Commun. Heat Mass Transf.* **123**, 105194 (2021).
17. Kumar, T. S. Hybrid nanofluid slip flow and heat transfer over a stretching surface. *Partial Differ. Equ. Appl. Math.* **4**, 100070 (2021).
18. Fazeli, I., Emami, M. R. S. & Rashidi, A. Investigation and optimisation of the behavior of heat transfer and flow of MWCNT-CuO hybrid nanofluid in a brazed plate heat exchanger using response surface methodology. *Int. Commun. Heat Mass Transf.* **122**, 105175 (2021).
19. Khashi'ie, N. S. *et al.* Flow and heat transfer past a permeable power-law deformable plate with orthogonal shear in a hybrid nanofluid. *Alex. Eng. J.* **59**(3), 1869–1879 (2020).
20. Rashid, U. *et al.* Study of (Ag and TiO<sub>2</sub>)/water nanoparticles shape effect on heat transfer and hybrid nanofluid flow toward stretching shrinking horizontal cylinder. *Results Phys.* **21**, 103812 (2021).
21. Salman, S., Abu Talib, A. R., Saadon, S. & Hameed-Sultan, M. T. Hybrid nanofluid flow and heat transfer over backward and forward steps: A review. *Powder Technol.* **363**, 448–472 (2020).
22. Alizadeh, R. *et al.* A machine learning approach to the prediction of transport and thermodynamic processes in multiphysics systems—Heat transfer in a hybrid nanofluid flow in porous media. *J. Taiwan Inst. Chem. Eng.* **124**, 290–306 (2021).
23. Ekiciler, R. & Cetinkaya, M. S. A. A comparative heat transfer study between monotype and hybrid nanofluid in a duct with various shapes of ribs. *Therm. Sci. Eng. Prog.* **23**, 100913 (2021).
24. Ahmed, W. *et al.* Heat transfer growth of sonochemically synthesised novel mixed metal oxide ZnO+Al<sub>2</sub>O<sub>3</sub>+TiO<sub>2</sub>/DW based ternary hybrid nanofluids in a square flow conduit. *Renew. Sustain. Energy Rev.* **145**, 111025 (2021).
25. Dagonchi, A. S. & Ganji, D. D. Impact of Cattaneo-Christov heat flux on MHD nanofluid flow and heat transfer between parallel plates considering thermal radiation effect. *J. Taiwan Inst. Chem. Eng.* **80**, 52–63 (2017).
26. Muhammad, N., Nadeem, S. & Mustafa, T. Squeezed flow of a nanofluid with Cattaneo-Christov heat and mass fluxes. *Results Phys.* **7**, 862–869 (2017).
27. Sultana, U., Mushtaq, M., Muhammad, T. & Albakri, A. On Cattaneo-Christov heat flux in carbon-water nanofluid flow due to stretchable rotating disk through porous media. *Alex. Eng. J.* (2021) (in press). <https://doi.org/10.1016/j.aej.2021.08.065>
28. Yahya, A. U. *et al.* Implication of bio-convection and Cattaneo-Christov heat flux on Williamson Sutterby nanofluid transportation caused by a stretching surface with convective boundary. *Chin. J. Phys.* **73**, 706–718 (2021).
29. Ibrahim, W., Dessale, A. & Gamachu, D. Analysis of flow of visco-elastic nanofluid with third order slips flow condition, Cattaneo-Christov heat and mass diffusion model. *Propuls. Power Res.* **10**(2), 180–193 (2021).
30. Ali, B., Pattnaik, P. K., Naqvi, R. A., Waqas, H. & Hussain, S. Brownian motion and thermophoresis effects on bioconvection of rotating Maxwell nanofluid over a rigid plate with Arrhenius activation energy and Cattaneo-Christov heat flux theory. *Therm. Sci. Eng. Prog.* **23**, 100863 (2021).

31. Li, Y. *et al.* Bio-convective Darcy–Forchheimer periodically accelerated flow of non-Newtonian nanofluid with Cattaneo–Christov and Prandtl effective approach. *Case Stud. Therm. Eng.* **26**, 101102 (2021).
32. Tong, Z. *et al.* Non-linear thermal radiation and activation energy significances in slip flow of bioconvection of Oldroyd-B nanofluid with Cattaneo–Christov theories. *Case Stud. Therm. Eng.* **26**, 101069 (2021).
33. Ali, B., Hussain, S., Nie, Y., Hussein, A. K. & Habib, D. Finite element investigation of Dufour and Soret impacts on MHD rotating flow of Oldroyd-B nanofluid over a stretching sheet with double diffusion Cattaneo Christov heat flux model. *Powder Technol.* **377**, 439–452 (2021).
34. Waqas, H., Muhammad, T., Noreen, S., Farooq, U. & Alghamdi, M. Cattaneo–Christov heat flux and entropy generation on hybrid nanofluid flow in a nozzle of rocket engine with melting heat transfer. *Case Stud. Therm. Eng.* **28**, 101504 (2021) (in press).
35. Haneef, M., Nawaz, M., Alharbi, S. O. & Elmasry, Y. Cattaneo–Christov heat flux theory and thermal enhancement in hybrid nano Oldroyd-B rheological fluid in the presence of mass transfer. *Int. Commun. Heat Mass Transf.* **126**, 105344 (2021).
36. Reddy, M. G., Rani, M. V. V. N. L. S., Kumar, K. G., Prasannakumar, B. C. & Lokesh, H. J. Hybrid dusty fluid flow through a Cattaneo–Christov heat flux model. *Phys. A Stat. Mech. Appl.* **551**, 123975 (2020).
37. Yan, S. *et al.* The rheological behavior of MWCNTs-ZnO/water-ethylene glycol hybrid non-Newtonian nanofluid by using of an experimental investigation. *J. Mater. Res. Technol.* **9**(4), 8401–8406 (2020).
38. Nabwey, H. A. & Mahdy, A. Transient flow of micropolar dusty hybrid nanofluid loaded with Fe<sub>3</sub>O<sub>4</sub>-Ag nanoparticles through a porous stretching sheet. *Results Phys.* **21**, 103777 (2021).
39. Madhukesh, J. K. *et al.* Numerical simulation of AA7072-AA7075/water-based hybrid nanofluid flow over a curved stretching sheet with Newtonian heating: A non-Fourier heat flux model approach. *J. Mol. Liquids* **335**, 116103 (2021).
40. Esfe, M. H., Esfandeh, S., Kamyab, M. H. & Toghraie, D. Analysis of rheological behavior of MWCNT-Al<sub>2</sub>O<sub>3</sub> (10:90)/5W50 hybrid non-Newtonian nanofluid with considering viscosity as a three-variable function. *J. Mol. Liquids* **341**, 117375 (2021).
41. He, W. *et al.* Using of Artificial Neural Networks (ANNs) to predict the thermal conductivity of Zinc Oxide–Silver (50%–50%)/Water hybrid Newtonian nanofluid. *Int. Commun. Heat Mass Transf.* **116**, 104645 (2020).
42. Hussain, A., Maliki, M. Y., Awais, M., Salahuddin, T. & Bilal, S. Computational and physical aspects of MHD Prandtl–Eyring fluid flow analysis over a stretching sheet. *Neural Comput. Appl.* **31**, 425–433 (2019).
43. Ur-Rehman, K., Malik, A. A., Malik, M. Y., Tahir, M. & Zehra, I. On new scaling group of transformation for Prandtl–Eyring fluid model with both heat and mass transfer. *Results Phys.* **8**, 552–558 (2018).
44. Khan, M. I., Alsaedi, A., Qayyum, S., Hayat, T. & Khan, M. I. Entropy generation optimisation in flow of Prandtl–Eyring nanofluid with binary chemical reaction and Arrhenius activation energy. *Colloids Surf. A* **570**, 117–126 (2019).
45. Akram, J., Akbar, N. S. & Maraj, E. Chemical reaction and heat source/sink effect on magnetonano Prandtl–Eyring fluid peristaltic propulsion in an inclined symmetric channel. *Chin. J. Phys.* **65**, 300–313 (2020).
46. Li, Y. *et al.* An assessment of the mathematical model for estimating of entropy optimised viscous fluid flow towards a rotating cone surface. *Sci. Rep.* **11**, 10259 (2021).
47. Jamshed, W. *et al.* Thermal growth in solar water pump using Prandtl–Eyring hybrid nanofluid: A solar energy application. *Sci. Rep.* **11**, 18704 (2021).
48. Keller, H. B. & Cebeci, T. Accurate numerical methods for boundary layer flows 1. Two dimensional flows. In *Proceeding International Conference Numerical Methods in Fluid Dynamics, Lecture Notes in Physics* (Springer, New York, 1971).
49. Cebeci, T. & Bradshaw, P. *Physical and Computational Aspects of Convective Heat Transfer* (Springer, 1984).
50. Bilal, S., Ur-Rehman, K. & Malik, M. Y. Numerical investigation of thermally stratified Williamson fluid flow over a cylindrical surface via Keller box method. *Results Phys.* **7**, 690–696 (2017).
51. Swalmeh, M. Z., Alkasasbeh, H. T., Hussanan, A. & Mamat, M. Heat transfer flow of Cu-water and Al<sub>2</sub>O<sub>3</sub>-water micropolar nanofluids about a solid sphere in the presence of natural convection using Keller-box method. *Results Phys.* **9**, 717–724 (2018).
52. Salahuddin, T. Carreau fluid model towards a stretching cylinder: Using Keller box and shooting method. *Ain Shams Eng. J.* **11**(2), 495–500 (2020).
53. Singh, K., Pandey, A. K. & Kumar, M. Numerical solution of micropolar fluid flow via stretchable surface with chemical reaction and melting heat transfer using Keller-box method. *Propul. Power Res.* **10**(2), 194–207 (2021).
54. Bhat, A. & Katagi, N. N. Magnetohydrodynamic flow of viscous fluid and heat transfer analysis between permeable discs: Keller-box solution. *Case Stud. Therm. Eng.* **28**, 101526 (2021).
55. Habib, D., Salamat, N., Hussain, S., Ali, B. & Abdal, S. Significance of Stephen blowing and Lorentz force on dynamics of Prandtl nanofluid via Keller box approach. *Int. Commun. Heat Mass Transf.* **128**, 105599 (2021).
56. Zeeshan, A., Majeed, A., Akram, M. J. & Alzahrani, F. Numerical investigation of MHD radiative heat and mass transfer of nanofluid flow towards a vertical wavy surface with viscous dissipation and Joule heating effects using Keller-box method. *Math. Comput. Simul.* **190**, 1080–1109 (2021).
57. Abbasi, A. *et al.* Implications of the third-grade nanomaterials lubrication problem in terms of radiative heat flux: A Keller box analysis. *Chem. Phys. Lett.* **783**, 139041 (2021).
58. Abbasi, A. *et al.* Optimised analysis and enhanced thermal efficiency of modified hybrid nanofluid (Al<sub>2</sub>O<sub>3</sub>, CuO, Cu) with non-linear thermal radiation and shape features. *Case Stud. Therm. Eng.* **28**, 101425 (2021).
59. Itikhar, N., Rehman, A. & Sadaf, H. Theoretical investigation for convective heat transfer on Cu/water nanofluid and (SiO<sub>2</sub>-copper)/water hybrid nanofluid with MHD and nanoparticle shape effects comprising relaxation and contraction phenomenon. *Int. Commun. Heat Mass Transf.* **120**, 105012 (2021).
60. Ijaz, S., Iqbal, Z. & Maraj, E. N. Mediation of nanoparticles in permeable stenotic region with infusion of different nanoshape features. *J. Therm. Anal. Calorim.* (2021). <https://doi.org/10.1007/s10973-021-10986-x>
61. Sahoo, R. R. Thermo-hydraulic characteristics of radiator with various shape nanoparticle-based ternary hybrid nanofluid. *Powder Technol.* **370**, 19–28 (2020).
62. Elnaqeeb, T., Animasaun, I. L. & Shah, N. A. Ternary-hybrid nanofluid: Significance of suction and dual-stretching on three-dimensional flow of water conveying nanoparticles with various shapes and densities. *Zeitschrift fur Naturforschung A* **76**(3), 231–243 (2021).
63. Rashid, U. *et al.* Study of (Aq and TiO<sub>2</sub>)/water nanoparticles shape effect on heat transfer and hybrid nanofluid flow towards stretching shrinking horizontal cylinder. *Results Phys.* **21**, 103812 (2021).
64. Jamshed, W. *et al.* A numerical frame work of magnetically driven Powell Eyring nanofluid using single phase model. *Sci. Rep.* **11**, 16500 (2021).
65. Mekheimer, K. S. & Ramadan, S. F. New insight into gyrotactic microorganisms for bio-thermal convection of Prandtl nanofluid over a stretching/shrinking permeable sheet. *SN Appl. Sci.* **2**, 450 (2020).
66. Jamshed, W. *et al.* Thermal growth in solar water pump using Prandtl–Eyring hybrid nanofluid: A solar energy application. *Sci. Rep.* **11**, 18704 (2021).
67. Aziz, A., Jamshed, W. & Aziz, T. Mathematical model for thermal and entropy analysis of thermal solar collectors by using Maxwell nanofluids with slip conditions, thermal radiation and variable thermal conductivity. *Open Phys.* **16**(1), 123–136 (2018).
68. Waqas, H., Hussain, M., Alqarni, M., Eid, M. R. & Muhammad, T. Numerical simulation for magnetic dipole in bioconvection flow of Jeffrey nanofluid with swimming motile microorganisms. *Waves Random Complex Media* 1–18 (2021). <https://doi.org/10.1080/17455030.2021.1948634>

69. Al-Hossainy, A. F. & Eid, M. R. Combined theoretical and experimental DFT-TDDFT and thermal characteristics of 3-D flow in rotating tube of [PEG+ H<sub>2</sub>O/SiO<sub>2</sub>-Fe<sub>3</sub>O<sub>4</sub>] C hybrid nanofluid to enhancing oil extraction. *Waves Random Complex Media* 1–26 (2021). <https://doi.org/10.1080/17455030.2021.1948631>
70. Ali, H. M. *Hybrid Nanofluids for Convection Heat Transfer* (Academic Press, 2020).
71. Jamshed, W. & Aziz, A. Cattaneo–Christov based study of TiO<sub>2</sub>–CuO/EG Casson hybrid nanofluid flow over a stretching surface with entropy generation. *Appl. Nanosci.* 8(4), 685–698 (2018).
72. Aziz, A., Jamshed, W., Aziz, T., Bahaidarah, H. M. S. & Rehman, K. U. Entropy analysis of Powell–Eyring hybrid nanofluid including effect of linear thermal radiation and viscous dissipation. *J. Therm. Anal. Calorim.* 143(2), 1331–1343 (2021).
73. Xu, X. & Chen, S. Cattaneo–Christov heat flux model for heat transfer of Marangoni boundary layer flow in a copper–water nanofluid. *Heat Transf. Asian Res.* 46(8), 1281–1293 (2017).
74. Muhammad, K., Hayat, T., Alsaedi, A. & Ahmed, B. A comparative study for convective flow of basefluid (gasoline oil), nanomaterial (SWCNTs) and hybrid nanomaterial (SWCNTs+MWCNTs). *Appl. Nanosci.* 11, 9–20 (2020).
75. Jamshed, W. *et al.* Computational frame work of Cattaneo–Christov heat flux effects on Engine Oil based Williamson hybrid nanofluids: A thermal case study. *Case Stud. Therm. Eng.* 26, 101179 (2021).
76. Brewster, M. Q. *Thermal Radiative Transfer and Properties* (Wiley, 1992).
77. Keller, H. B. A new difference scheme for parabolic problems. In *Numerical Solution of Partial Differential Equations-II*. (SYNSPADE 1970) (Proc. Sympos., Univ. of Maryland, College Park, Md., 1970), 327–350 (Academic Press, 1971).
78. Abolbashari, M. H., Freidoonimehr, N., Nazari, F. & Rashidi, M. M. Entropy analysis for an unsteady MHD flow past a stretching permeable surface in nano-fluid. *Powder Technol.* 267, 256–267 (2014).
79. Das, S., Chakraborty, S., Jana, R. N. & Makinde, O. D. Entropy analysis of unsteady magneto-nanofluid flow past accelerating stretching sheet with convective boundary condition. *Appl. Math. Mech.* 36(12), 1593–1610 (2015).
80. Jamshed, W., Devi, S. U. & Nisar, K. S. Single phase-based study of Ag-Cu/EO Williamson hybrid nanofluid flow over a stretching surface with shape factor. *Phys. Scr.* 96, 065202 (2021).
81. Jamshed, W. Thermal augmentation in solar aircraft using tangent hyperbolic hybrid nanofluid: A solar energy application. *Energy Environ.* 1–44 (2021). <https://doi.org/10.1177/0958305X211036671>
82. Jamshed, W. & Nisar, K. S. Computational single phase comparative study of williamson nanofluid in parabolic trough solar collector via Keller box method. *Int. J. Energy Res.* 45, 10696–10718 (2021).
83. Jamshed, W. & Aziz, A. A comparative entropy based analysis of Cu and Fe<sub>3</sub>O<sub>4</sub>/methanol Powell–Eyring nanofluid in solar thermal collectors subjected to thermal radiation, variable thermal conductivity and impact of different nanoparticles shape. *Results Phys.* 9, 195–205 (2018).
84. Jamshed, W. *et al.* Evaluating the unsteady Casson nanofluid over a stretching sheet with solar thermal radiation: An optimal case study. *Case Stud. Therm. Eng.* 26, 101148 (2021).

## Acknowledgements

This study was supported by Taif University Researchers Supporting Project Number (TURSP-2020/117), Taif University, Taif, Saudi Arabia.

## Author contributions

W.J. and F.S. framed the issue. W.J., D.B., N.A.A.M.N., F.S., and K.S.N. resolved the problem. W.J., F.S., N.A.A.M.N., K.S.N., M.S., S.A. and K.A.I. computed and analysed the results. All the authors equally contributed to the writing and proofreading of the paper.

## Competing interests

The authors declare no competing interests.

## Additional information

**Correspondence** and requests for materials should be addressed to W.J. or D.B.

**Reprints and permissions information** is available at [www.nature.com/reprints](http://www.nature.com/reprints).

**Publisher's note** Springer Nature remains neutral with regard to jurisdictional claims in published maps and institutional affiliations.



**Open Access** This article is licensed under a Creative Commons Attribution 4.0 International License, which permits use, sharing, adaptation, distribution and reproduction in any medium or format, as long as you give appropriate credit to the original author(s) and the source, provide a link to the Creative Commons licence, and indicate if changes were made. The images or other third party material in this article are included in the article's Creative Commons licence, unless indicated otherwise in a credit line to the material. If material is not included in the article's Creative Commons licence and your intended use is not permitted by statutory regulation or exceeds the permitted use, you will need to obtain permission directly from the copyright holder. To view a copy of this licence, visit <http://creativecommons.org/licenses/by/4.0/>.

© The Author(s) 2021